

2006

Time-Resolved Magneto-Optical Imaging of Superconducting YBCO Thin Films in the High-Frequency AC Current Regime

Alexander Frey
College of William & Mary - Arts & Sciences

Follow this and additional works at: <https://scholarworks.wm.edu/etd>



Part of the [Condensed Matter Physics Commons](#)

Recommended Citation

Frey, Alexander, "Time-Resolved Magneto-Optical Imaging of Superconducting YBCO Thin Films in the High-Frequency AC Current Regime" (2006). *Dissertations, Theses, and Masters Projects*. Paper 1539626846.

<https://dx.doi.org/doi:10.21220/s2-hn37-bk65>

This Thesis is brought to you for free and open access by the Theses, Dissertations, & Master Projects at W&M ScholarWorks. It has been accepted for inclusion in Dissertations, Theses, and Masters Projects by an authorized administrator of W&M ScholarWorks. For more information, please contact scholarworks@wm.edu.

TIME-RESOLVED MAGNETO-OPTICAL IMAGING OF SUPERCONDUCTING
YBCO THIN FILMS IN THE HIGH-FREQUENCY AC CURRENT REGIME

A Thesis

Presented To

The Faculty of the Department of Applied Science

The College of William and Mary in Virginia

In Partial Fulfillment

Of the Requirements for the Degree of

Master of Science


by

Alexander Frey


July 2006

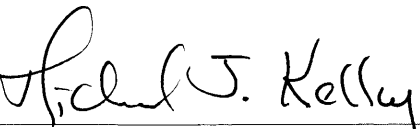
APPROVAL SHEET


This thesis is submitted in partial fulfillment of
the requirements for the degree of
Master of Science


Alexander Frey

Approved by the Committee, July 2006


Dr. Gunter Luepke,
Professor, Department of Applied Science


Dr. Michael J. Kelley
Professor, Department of Applied Science


Dr. William J. Kossler
Professor, Physics Department

Contents

Acknowledgements	iv
List of Figures	v
Abstract	x
1. Introduction	2
2. Theory	4
1. Introduction to Superconductors	4
2. Bean Critical State Model	11
3. Critical State Model for Thin Films.	14
3. Magneto-Optical Imaging (MOI)	22
1. Faraday Effect	22
2. Experimental Setup	25
1. Imaging Equipment	26
2. Synchronization	30
3. Calibration	31
4. Samples	33
4. Frequency Dependent Measurements	36
5. Phase Dependent Measurements	45
6. Conclusions	61
Appendix A – Synchronization	62
Appendix B – Inversion	66
References	68
Vita	70

Acknowledgements

The author wishes to express his appreciation to Professor Gunter Luepke, under whose supervision this investigation was conducted, for his patient guidance and criticism throughout the investigation. The author is indebted to Dr. Andrea Lucarelli for guidance in the investigation and valuable discussion. The author would also like to thank Professors Michael J. Kelley and William J. Kossler for their careful reading and criticism of the manuscript.

List of Figures

1	Magnetization curve for type I and type II superconductors. The <i>negative</i> of the magnetization is plotted on the positive Y axis.	5
2	Phase diagram for type II superconductors.	6
3	Flux lines that are penetrating a type II superconductor in the mixed state $H_{c1} < H < H_{c2}$	7
4	Demagnetization effects in a long rod with magnetic field applied parallel to its axis, for a spherical sample and a thin film sample with perpendicular field. In the rod demagnetization can be neglected, not so in the sphere and in the thin film. The field on the equatorial circle of the sphere can be analytically determined to be $H = 3/2 \times H_a$	8
5	Repulsive interaction between two flux lines due to the Lorentz force. The magnetic field in both flux lines is directed into the plane of the drawing.	9
6	Sketch of the slab geometry used in the Bean model. If a magnetic field $B_a > B_{c1}$ is applied parallel to a slab, flux lines penetrate into the slab up to a depth $w - a$, given by the critical current density.	11
7	Magnetic flux density $B_z(x)$ and current density $J_y(x)$ profiles across a slab in the Bean model, for monotonically increased applied fields B_a	13
8	Field and current profile in a slab if the applied field is reversed from $B_a = +0.6B_s$ to $-0.8B_s$	13
9	Diagram of a thin film superconductor with $d \ll w$ and infinite length in a perpendicular magnetic field.	14
10	Field and current density distribution in a thin film in different applied fields B_a , calculated from the critical state model.	16
11	Current distribution in a thin film if only a transport current is applied.	17
12	Plot of the transport current distribution according to Eq. 19, for different values of the applied current $I_T = 0.09I_c, 0.44I_c, 1.78I_c$	19

13	Current (top) and flux density (bottom) distribution in the case of an applied field and a <i>small</i> transport current $I_T = 0.09I_c$	19
14	Current (top) and flux density (bottom) distribution in the case of an applied field and a <i>medium</i> transport current $I_T = 0.44I_c$	20
15	Current (top) and flux density (bottom) distribution in the case of an applied field and a <i>high</i> transport current $I_T = 1.78I_c$	21
16	The ferrite-garnet based magneto-optical indicator. The polarization direction of light passing through the indicator layer is rotated by an angle Θ_F proportional to the local perpendicular magnetic field.	24
17	MOI setup. As light sources a Hg-vapor lamp and a pulsed laser are available, but only the laser can be synchronized to the AC current source in order to take stroboscopic time dependent measurements.	26
18	Spectral sensitivity of the camera. The wavelength of the laser is $\lambda = 527nm$. 28	
19	Block diagram of the synchronization scheme. The phase of the AC current at which laser pulses are triggered is adjusted with a home-built synchronization circuit. The laser pulses are detected with a photodiode and are displayed on an oscilloscope together with the transport current signal, in order to control the relative phase.	30
20	Magneto-optical image used for calibration. The field on this image is $B = 65mT$	33
21	Calibration curve for quantitative magneto-optical measurements. The temperature is $T = 18K$, the laser prf is $1000Hz$, and the exposure time of the camera is $\tau = 20ms$	34
22	Optical micrograph of a YBCO sample.	35
23	DC resistance versus temperature curve for a YBCO thin film sample. . . .	36

24	Magneto-optical images of the bridge at $f = 1000Hz$, taken at the maximum, zero and minimum phase points of the AC current. The intensity profiles obtained by averaging parallel to the bridge are shown below the images.	37
25	Intensity of MOI images versus the number of collected light pulses, which is given by the product of current frequency and exposure time. A y-axis offset $B = 13.8 \pm 1.4$ is obtained from a linear fit, it is needed as a parameter in the exposure time correction with equation 26.	38
26	Frequency dependent intensity profiles at maximum AC current. The broken lines mark the edges of the sample.	39
27	Frequency dependent intensity profiles at zero phase point of the AC current. The broken lines mark the edges of the sample.	39
28	Intensity profiles across the bridge for different frequencies at the minimum of the transport current.	40
29	Normalized intensity profiles for different frequencies at maximum transport current.	41
30	Normalized intensity profiles for different frequencies at the zero phase point of the transport current.	42
31	Normalized intensity profiles for different frequencies at the minimum of the transport current.	42
32	Magnetic flux density profiles across the bridge for different frequencies at maximum transport current. The flux density has been manually set to $B = 0mT$ in the sample center.	43
33	Magnetic flux density profiles across the bridge for different frequencies at the zero phase point of the transport current. The flux density has been manually set to $B = 0mT$ in the sample center.	43

34	Magnetic flux density profiles across the bridge for different frequencies at the minimum of the transport current. The flux density has been manually set to $B = 0mT$ in the sample center.	44
35	B-field profiles for the first half of the current period.	47
36	B-field profiles for the second half of the current period.	47
37	B-field profiles with focus on one sample edge for both half cycles.	48
38	Current density profiles for the first half of the current phase.	49
39	Current density profiles for the second half of the current phase.	50
40	AC current through the sample. Black: applied current in the experiment, with an amplitude of $8.54A$. Red: current obtained by integration of MOI current density profiles, with an amplitude of $5.92A$	50
41	Current density profile calculated assuming different values for the distance between h sample and indicator. $h = 0.01w \approx 0.35\mu m$	51
42	Experimental and theoretical flux density profile at maximum transport current. The theoretical curve is calculated assuming a current $I_T = 8.54A$	53
43	Experimental and theoretical flux density profile at minimum transport current. The theoretical curve is calculated assuming a current $I_T = -8.54A$	53
44	Experimental and theoretical flux density profile at zero transport current.	56
45	Experimental and theoretical flux density profile at intermediate transport current.	56
46	Experimental and theoretical flux density profile at maximum transport current. The range where the experiment shows a higher flux penetration than predicted by the model is marked, as well as the maximum difference in this region between the experimental and the theoretical flux density.	57
47	Experimental and theoretical flux density profile at negative intermediate transport current.	57
48	Experimental and theoretical flux density profile at minimum transport current.	58

49	Experimental and theoretical current density profile at zero transport current.	58
50	Experimental and theoretical current density profile at intermediate transport current.	59
51	Experimental and theoretical current density profile at maximum transport current.	59
52	Experimental and theoretical current density profile at negative intermediate transport current.	60
53	Experimental and theoretical flux density profile at minimum transport current.	60
54	Schematic of the first delay stage	63
55	Schematic of the second delay stage	64
56	Schematic of the stabilization of the power supply for the synchronization .	65

Abstract

Time-resolved quantitative magneto-optical imaging has been used to study the magnetic flux density and current density distribution in a $\text{Yb}_2\text{Cu}_3\text{O}_{7.6}$ thin film at $T = 24\text{K}$, as a function of the frequency and the phase of an applied AC transport current. In the range from 100Hz to 1000Hz no changes in the flux distribution with the AC frequency have been observed.

The phase dependent flux distribution can be described with an extended critical state model, which assumes that the transport current distributes in the sample in such a way, that the self field inside the sample is zero. The total current distribution is given by the sum of the time dependent transport current and the shielding current due to an external magnetic field. Deviations from this model can be attributed to thermally activated flux creep.

TIME-RESOLVED MAGNETO-OPTICAL IMAGING OF SUPERCONDUCTING
YBCO THIN FILMS IN THE HIGH-FREQUENCY AC CURRENT REGIME

1 Introduction

The development of high temperature superconductors for technical applications has made great progress in recent years, the introduction of economic manufacturing processes for $YBa_2Cu_3O_{7-\delta}$ (YBCO) based superconducting cables brings practical applications closer [1]. The range of applications is wide: In the electric power grid high temperature superconducting cables can reduce energy losses, used in the coils of electric motors and generators they increase the efficiency while at the same time reducing size and weight of those engines [2, 3]. In most applications the superconductors will be in the form of thin strips which are exposed to external magnetic fields and are used to carry AC currents with frequencies up to 1000Hz. To understand and to optimize the electric and magnetic properties of high temperature superconductors under these conditions, the spatial distribution of the magnetic field and the current density plays an important role.

Studies of the spatial distribution of the magnetic field in thin films of high temperature superconductors have been done using magneto-optical imaging techniques [4, 5, 6]. The results are commonly interpreted in terms of the critical state model [7, 8, 9]. However, those studies have been limited to static measurements, such as constant magnetic field and DC applied current, or to measurements under rather slowly evolving conditions like thermal relaxation of magnetic flux in the remanent state. Dynamic studies with high time resolution in the practically important case of high frequency alternating currents have not been done yet. There are effects that can potentially result in a difference between the flux distribution in the AC and in static regimes:

In low temperature superconductors a non-equilibrium penetration of magnetic flux has recently been observed [10]. Triggered by local thermo-magnetic instabilities, flux lines can penetrate into the material locally in large quantities and on a very short time scale. If these so called flux jumps occur in YBCO conductors under the influence of an AC current with a period comparable to the timescale of the jumps, this could lead to a different flux penetration into the material than in static cases and potentially also mean a frequency dependence of the flux distribution [11].

A second relevant effect is the well known thermal relaxation of the magnetic flux distribution inside type II superconductors. Although relaxation usually takes place on longer time scales, it could possibly lead to a different flux distribution for different frequencies of an applied current.

Motivated by these questions, this work has the following objectives:

- Determine if the flux distribution inside a thin film of $YBa_2Cu_3O_{7-\delta}$ changes with the frequency of an applied current in the practically important range of 100Hz to 1000Hz.
- Measure the spatial distribution of magnetic flux density and current density as a function of the phase of the applied current, and compare the results to the predictions of the critical state model.

To achieve this, a time-resolved magneto-optical imaging technique has been developed with contributions from this work. It is capable of measuring cyclic magnetic flux distributions in planar superconductors carrying alternating current with frequencies up to 1000Hz, with high spatial resolution.

The thesis is organized as follows: In section 2 a general introduction to the behavior of superconductors in magnetic fields is given and the critical state model is outlined. Flux and current distributions relevant for this work as predicted by the critical state model are given. In section 3 an introduction to the magneto-optical imaging technique in general is given, and the experimental setup used in this work is presented. The results of the frequency dependent and the phase dependent studies are presented in sections 4 and 5, and are summarized in the conclusion in section 6.

2 Theory

2.1 Introduction to Superconductors

The most distinguishing and well known property of superconductors is the loss of electric resistivity when they are cooled below a material dependent transition temperature T_c . Elementary superconductors, such as Pb, Nb, Hg, have transition temperatures $T_c \leq 9.5K$, whereas complex high temperature superconductors such as $YBa_2Cu_3O_7$ with $T_c = 92K$ have transition temperatures well above the boiling point of liquid nitrogen at $77.35K$. For the remaining resistivity in the superconducting state only an upper bound on the order of $\rho < 10^{-25}\Omega m$ can be experimentally determined, the theoretical value is $\rho = 0$. However, there are certain conditions under which superconductors exhibit a finite electric resistance, this effect will be discussed later in this section.

The second distinguishing feature of superconductors is their behavior in magnetic fields. Since $\rho \approx 0$, one expects that superconductors behave like ideal diamagnets with a magnetic susceptibility $\chi = -1$. If a magnetic field H_a is applied, a macroscopic current flowing along the sample surface is induced. Since it is not attenuated by electric resistance, the induced current creates a magnetization $M \equiv -H_a$, thus *completely* shielding the field from the bulk of the superconductor. But superconductivity is more than just $\rho = 0$, and based on their different response to applied magnetic fields two types of superconductors can be distinguished. The magnetization curve for both types is shown in figure 1.

Type I : Superconductors of this type behave like ideal diamagnets for applied magnetic fields $H_a < H_c$, where H_c is a material and temperature dependent critical field. Macroscopic shielding currents flow around the sample in a thin surface layer with a thickness of the London penetration depth λ and expel the field completely from the bulk of the sample. If $H_a > H_c$ superconductivity breaks down and the sample assumes the normal conducting state with $M = 0$. The magnetization curve of a type I superconductor is

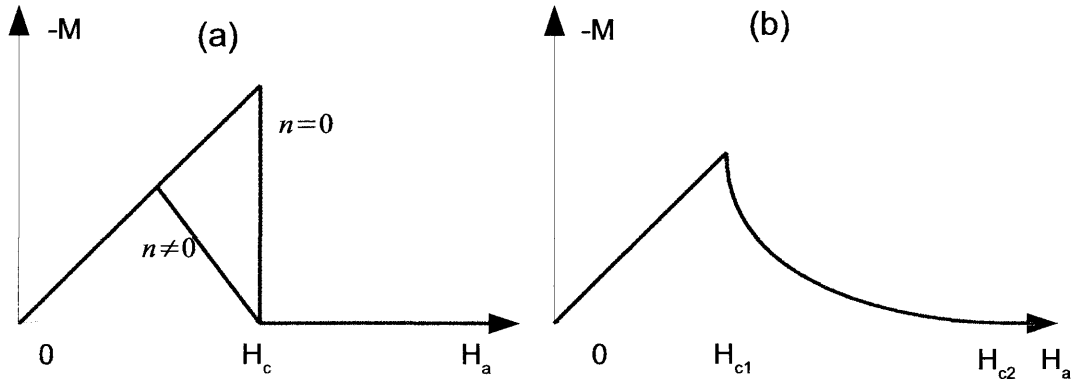


Figure 1: Magnetization curve for type I and type II superconductors. The *negative* of the magnetization is plotted on the positive Y axis.

displayed in figure 1(a). Most elemental superconductors such as *Hg*, *Pb* and *Al* belong to this type.

The abrupt breakdown of superconductivity from $M = -H_a$ to $M = 0$ at a precise magnetic field $H_a = H_c$ is an idealized behavior, which is observed only if demagnetization effects can be neglected. In general, a demagnetization factor $0 < n < 1$ has to be considered and superconductivity vanishes gradually in the range $(1 - n)H_c \leq H_a \leq H_c$. Demagnetization effects are described briefly later in this section, but since type I materials are not in the focus of this work, the breakdown of superconductivity in this case is not discussed further.

Type II : For magnetic fields less than a lower critical field H_{c1} these materials behave like type I superconductors. Above this threshold magnetic flux penetrates the bulk of the superconductor in a quantized way in the form single flux lines while the sample remains in the superconducting state. As the applied field is increased more flux lines enter the the sample and the magnetization is reduced gradually (Fig. 1(b)). Once the applied field reaches an upper critical field H_{c2} the density of flux lines inside the sample assumes its maximum, and superconductivity breaks down. Some elemental superconductors, such as *Nb*, and *C* in the form of nanotubes, as well as the technically important class of high

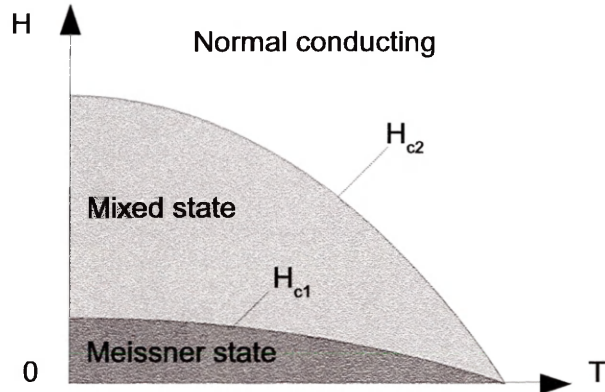


Figure 2: Phase diagram for type II superconductors.

temperature superconductors, which are in the focus of this work, are of this type. In the following a summary of the most important properties of type II superconductors is given.

The phase diagram of a type II superconductor in the plane $H(T)$ is shown in Fig. 2. Both critical fields are material and temperature dependent with $H_{c1,c2}(T) \rightarrow 0$ as $T \rightarrow T_c, T < T_c$. For $H < H_{c1}(T)$ the magnetic field is shielded completely from the bulk and the sample is said to be in a complete Meissner state. The state between $H_{c1}(T)$ and $H_{c2}(T)$, where the sample is partially penetrated by magnetic flux lines, is called the mixed state. For fields above $H_{c2}(T)$ the sample is in the normal conducting state.

In high temperature superconductors H_{c1} and H_{c2} also depend on the orientation of the field relative to the crystal growth axis \vec{c} , which is due to the layered crystal structure of these materials. For $YBa_2Cu_3O_7$ single crystals the lower critical field at $T = 0K$ lies between $H_{c1}(0) = 200Oe$ for $\vec{H} \parallel \vec{c}$ and $H_{c1}(0) = 1100Oe$ for $\vec{H} \perp \vec{c}$ [12]. The upper critical field in high temperature superconductors is generally very high, which is another advantage in technical applications besides their high T_c . In single crystalline $YBa_2Cu_3O_7$ at $T \rightarrow 0K$ the upper critical field is $\mu_0 H_{c2} > 100T$ for the field orientation $\vec{H} \perp \vec{c}$ [13].

Demagnetization effects Depending on the shape of the sample, demagnetization effects can become important for the magnetization behavior of a superconductor. De-

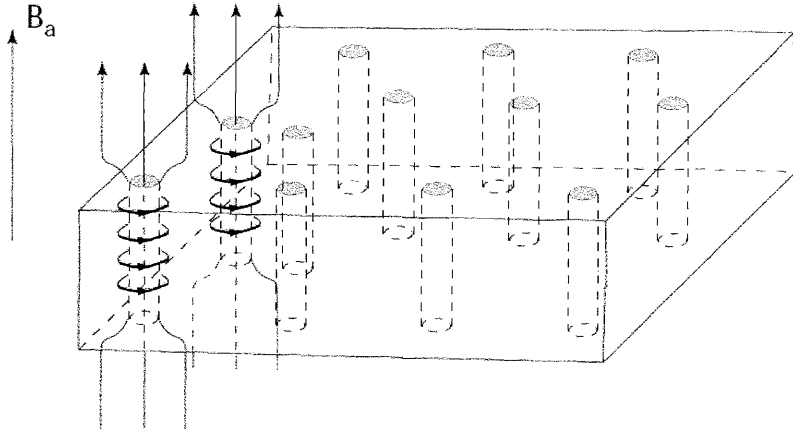


Figure 3: Flux lines that are penetrating a type II superconductor in the mixed state $H_{c1} < H < H_{c2}$

magnetization describes the increase of the magnetic field immediately outside the sample due to the flux that is expelled from the inside and which has to bend around the sample. Since $\chi = -1$ in the Meissner state, this effect is much stronger in superconductors than in normal diamagnetic metals, where $|\chi| \leq 10^{-4}$.

In Fig. 4 the distribution of magnetic field lines around superconducting samples with different geometries is shown. For a long, thin rod with a magnetic field applied parallel to its axis, the field is homogeneous along the sample surface except at the ends, and demagnetization can be neglected. For a spherical sample it can be shown[14] that due to the bending of flux lines the field on the equatorial circle is higher than the applied field by a factor of 3/2, and demagnetization can not be neglected. For a thin film sample with the magnetic field applied perpendicular to its surface, as it is the case in the experiments described in this work, field lines are also strongly bent around the sample and the increase of the magnetic field at the edges outside the sample can also not be neglected.

Vortices — In the mixed state between H_{c1} and H_{c2} , the magnetic field penetrates the bulk of a type II superconductor in the form of quantized flux lines (Fig. 3). Each line contains an amount of flux that is an integer multiple of the flux quantum $\phi_0 = h/2e$, where h is the Planck constant and e is the elementary charge. In the center of a flux

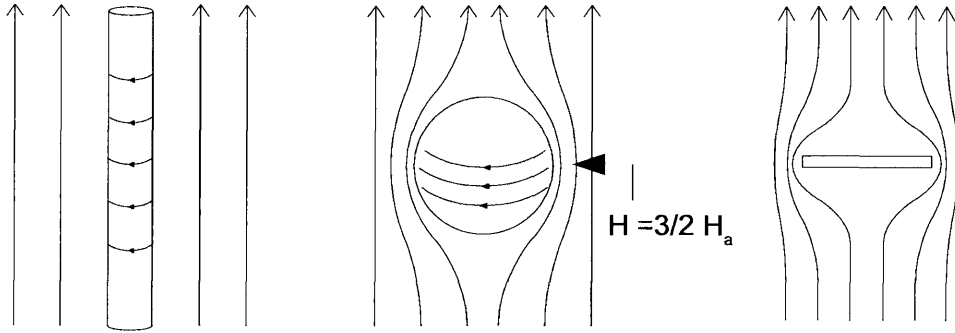


Figure 4: Demagnetization effects in a long rod with magnetic field applied parallel to its axis, for a spherical sample and a thin film sample with perpendicular field. In the rod demagnetization can be neglected, not so in the sphere and in the thin film. The field on the equatorial circle of the sphere can be analytically determined to be $H = 3/2 \times H_a$.

line the material is in the normal conducting phase and magnetic field lines can exist. Surrounding this region there are circular shielding currents flowing, which enclose the field lines in the center. Because of the shape of the shielding currents flux lines are also called vortices.

Vortices interact with each other via the Lorentz force that the shielding currents of one vortex exert on the magnetic flux enclosed in another vortex [14] :

$$\vec{F} = \vec{J} \times \vec{\Phi}_0. \quad (1)$$

Here \vec{F} is the Lorentz force per unit length on a flux line, \vec{j} is the current density at the position of the flux line due to the vortex current of a neighboring flux line, and $\vec{\Phi}_0$ is the flux enclosed in one line times its direction. The Lorentz force leads to a repulsive interaction between flux lines, as shown in Fig. 5. Because of this repulsion, the equilibrium distribution of flux lines in an ideal type II superconductor is a crystalline lattice, with flux lines situated at the corners of equilateral triangles.

Flux lines also experience a Lorentz force if a transport current is flowing through the superconductor. The force per unit volume \vec{F} acting on a flux line lattice with an

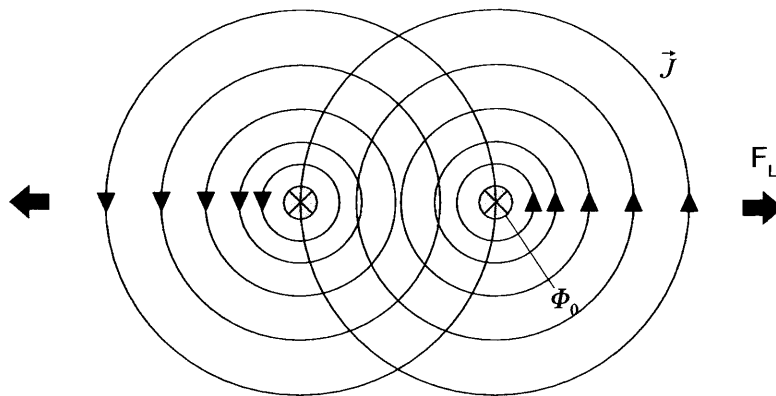


Figure 5: Repulsive interaction between two flux lines due to the Lorentz force. The magnetic field in both flux lines is directed into the plane of the drawing.

averaged magnetic flux density \vec{B} is

$$\vec{F}(\vec{r}) = \vec{J}(\vec{r}) \times \vec{B}(\vec{r}) \quad (2)$$

where \vec{J} is the transport current density. The Lorentz force acts equally on the flux line lattice and on the electrons carrying the transport current. Since the current is fixed by the boundaries of the sample, flux lines are forced to move through the sample perpendicular to the transport current. In an ideal type II superconductor, magnetic flux lines would thus continuously enter the sample on one edge, traverse the sample and exit it on the other edge.

Energy losses — The movement of flux lines in a superconductor in the presence of a transport current is connected to an energy loss from the current, and thus to an electric resistance. When the normal conducting core of a flux line is moving through the superconductor, the material right in front of the flux line undergoes a phase transition from the superconducting phase to the normal phase, and back again, once the flux line has passed. The phase transition costs energy if the flux line moves quickly, and the energy is taken from the transport current that drives the flux line. Another reason for the loss of energy lies in the acceleration of non-superconducting electrons due to a local electric

field that is generated by a moving magnetic flux line. The accelerated normal conducting electrons give their kinetic energy back to the crystal lattice and heat is generated. As a consequence of these effects, an ideal type II superconductor always has a finite resistance.

Pinning — The above discussion assumes that flux lines are moving freely through the superconductor and the only force acting on them is the Lorentz force. However, this is true only for idealized superconductors without any material defects. In a realistic superconductor, there are always defects in the crystal structure and in the material composition, which degrade the superconducting phase locally and create small regions where the material stays normal conducting even below T_c . Since the creation of flux lines in a superconductor costs energy, there is an energetic advantage if a flux line passes through such regions with normal conductivity, thus shortening the effective length of the flux line in the superconducting material. Because of this energy gain, defects in the superconductor act as potential wells for flux lines, also called pinning sites.

The Lorentz force acting on a flux line lattice has to be greater than the maximum pinning force F_p in order to move flux lines. The current density corresponding to the value where the Lorentz force equals F_p is called the critical current density J_c . From equation 2 one obtains

$$J_c(\vec{r}, \vec{B}) = \frac{F_p(\vec{r})}{|B(\vec{r})|} \quad (3)$$

If the pinning force is assumed to be homogeneous throughout the material, the critical current density is inversely proportional to the local magnetic flux field.

If a magnetic field $H > H_{c1}$ is applied to a type II superconductor, flux lines enter the material and are trapped in pinning sites close to the edges of the sample. They move further inside the sample if the repulsive force from following flux lines is greater than the maximum pinning force, which creates a gradient in the magnetic field inside the sample. The magnetic field distribution inside a type II superconductor can then be calculated from the Maxwell equation

$$\nabla \times \vec{B} = \mu_0 \vec{J}(\vec{r}), \quad (4)$$

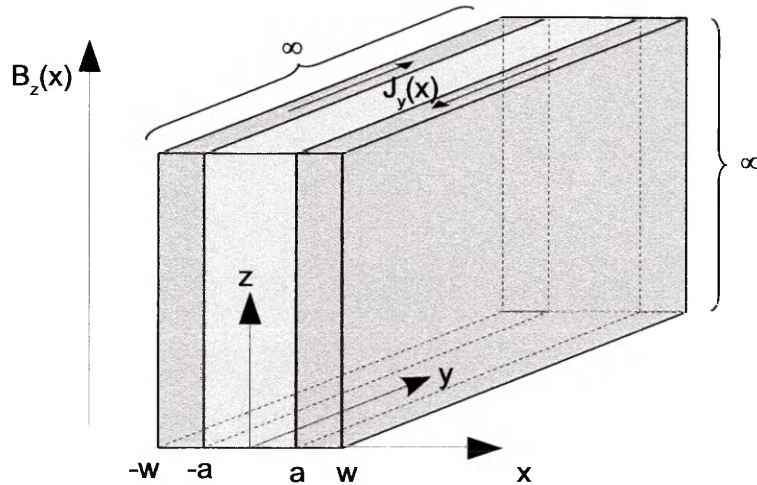


Figure 6: Sketch of the slab geometry used in the Bean model. If a magnetic field $B_a > B_{c1}$ is applied parallel to a slab, flux lines penetrate into the slab up to a depth $w - a$, given by the critical current density.

where

$$|\vec{J}(\vec{r})| = J_c(\vec{r}, \vec{B}). \quad (5)$$

Because the critical current density in general depends on the magnetic field, finding the magnetic flux distribution in this case is not trivial.

2.2 Bean Critical State Model

A widely used model to calculate the magnetic flux distribution inside a type II superconductor is the critical state model proposed by C. P. Bean [7]. It is based on the assumption that J_c is a material dependent constant which is *independent* of the local magnetic field $B(\vec{r})$. This is in contrast to equation 3, but it can be justified if the magnetic field is lower than the upper critical field of the material, as it is mostly the case in high temperature superconductors with their large H_{c2} . A second assumption being made is that $\vec{H} = \vec{B}/\mu_0$ inside the superconductor. This is justified if the applied field is significantly higher than the lower critical field H_{c1} .

Consider the geometry of a superconducting slab of width $2w$ in the x direction, with

infinite length and infinite height in the y and z directions (Fig. 6). A magnetic field $B_a > B_{c1}$ is applied in the z -direction parallel to the slab. Demagnetization can be neglected in this case and the magnetic field is constant everywhere outside the slab. Since in this geometry $\vec{B}(\vec{r}) \parallel \hat{z}$ Ampere's law (Eq.4) becomes

$$-\frac{\partial B_z(x)}{\partial x} = \mu_0 J_y(x). \quad (6)$$

When B_a is increased above B_{c1} , flux lines start to penetrate from the sample edges and they move into the sample as long as the repulsion from other flux lines is greater than the pinning force corresponding to J_c . They stop moving as soon as a flux distribution has been reached with $|\vec{J}(\vec{r})| \leq J_c$ everywhere where flux lines are present. The current density entering equation 6 must therefore be J_c , and the current and field distributions inside the slab are given by

$$J_y(x) = \begin{cases} J_c & -w \leq |x| < -a \\ 0 & 0 \leq |x| \leq a \\ -J_c & a < |x| \leq w \end{cases} \quad (7)$$

$$B_z(x) = \begin{cases} 0 & 0 \leq |x| \leq a \\ \mu_0(|x| - a)J_c & a < |x| \leq w \\ B_a & |x| > w. \end{cases} \quad (8)$$

The current and B-field distributions are depicted in Fig. 7. The length a is the half-width of a region in the center of the slab, into which flux lines have not yet penetrated at a given applied field. It is given by

$$a = w \left(1 - \frac{B_a}{B_s} \right), \quad (9)$$

where a decreases linearly with the applied field, and the slab is fully penetrated by magnetic flux lines at a characteristic field $B_s = \mu_0 w J_c$. In the field free region the

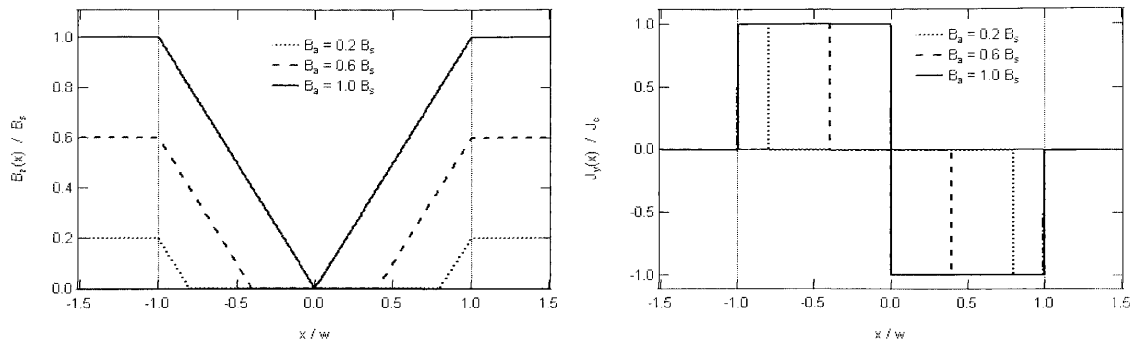


Figure 7: Magnetic flux density $B_z(x)$ and current density $J_y(x)$ profiles across a slab in the Bean model, for monotonically increased applied fields B_a .

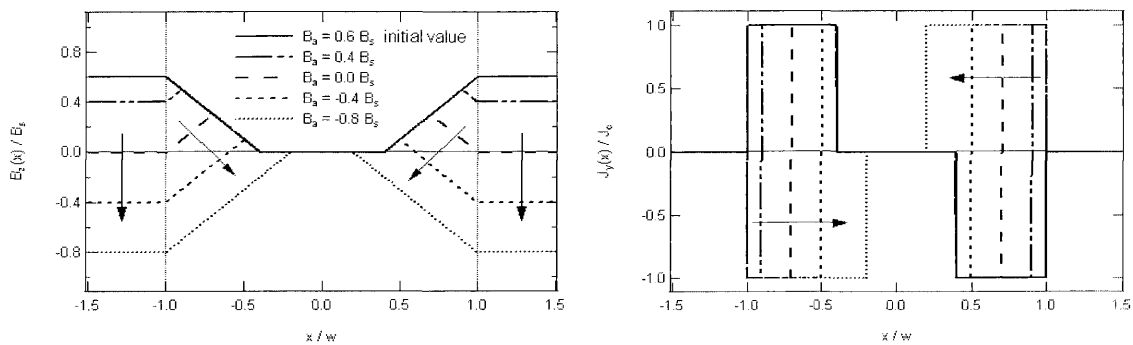


Figure 8: Field and current profile in a slab if the applied field is reversed from $B_a = +0.6B_s$ to $-0.8B_s$.

magnetic field is shielded by the screening current J_c flowing between the field free region and the slab surfaces.

The above case only holds if a sample is initially in the pure Meissner state, and the magnetic field is increased monotonically. In general, the flux distribution inside a type II superconductor strongly depends on the magnetic history of the sample. If, for example, the field is first ramped up monotonically and is then decreased to zero, an amount of flux stays pinned inside the slab and keeps a remanent magnetization. As an example, the field and current distribution in a slab is shown in Fig. 8 for the case of an applied field ramped from $B_a = 0.6B_s$ down to $B_a = -0.8B_s$.

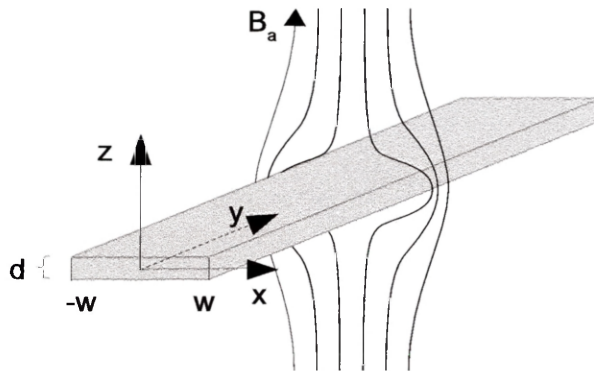


Figure 9: Diagram of a thin film superconductor with $d \ll w$ and infinite length in a perpendicular magnetic field.

2.3 Critical State Model for Thin Films

The Bean model as described in the previous section is good to introduce the general idea $J(y) = J_c = \text{const}$, but its results only hold for the geometry of an infinite slab with parallel magnetic field. However, this work is concerned with thin film superconductors, and a slightly different model that gives current and field density profile across the sample is needed.

Consider an infinitely long strip of a type II superconductor of thickness d and half width w in a perpendicular magnetic field (Fig. 9). It is assumed that $d \ll w$, but d can be larger than the London penetration depth λ of a Meissner screening current.

The current density in this case is one dimensional, and Ampere's law (Eq. 4) becomes

$$\mu_0 J_y(x) = \frac{\partial B_x}{\partial z} - \frac{\partial B_z}{\partial x}. \quad (10)$$

Because of demagnetization effects the magnetic field around the sample is strongly curved, and the term $\frac{\partial B_z}{\partial x}$ can not be neglected as it has been in the Bean model. However, the basic assumption $J_c = \text{const}$ of the Bean model can still be used.

To calculate the shielding current distribution in a thin superconductor film when a perpendicular field B_a is applied, one assumes that there is a constant current with density $J_y(x) = J_c$ flowing in the outer parts of the strip $a < x < w$, where a is the half-width of

a field free region in the center. This current creates a magnetic field $B(x) \neq 0$ inside the strip, which in turn has to be shielded by a current in the field free region. The current in the field free region does not have the requirement $J_y(x) = J_c$, since it flows only as a response to the current on the outside and is not accompanied by flux penetration. It still has to be determined.

Conformal mapping methods can be used to obtain the distribution of the shielding current in the field free region [8]. The field free region with half width a is mapped onto a circular cylinder of radius $a/2$ by a Joukowski transform. Then the shielding current on the cylinder surface parallel to its axis is calculated, which shields the inside from the field generated by a constant current density J_c flowing outside the cylinder. Mapping the current distribution back onto the thin film yields an analytic expression for the current in the field free region, and one obtains the total current density in the thin film

$$J_y(x) = \begin{cases} J_c & -w < x \leq -a \\ \frac{-2J_c}{\pi} \arctan\left(\frac{x}{w} \sqrt{\frac{w^2 - a^2}{a^2 - x^2}}\right) & -a < x < a \\ -J_c & a \leq x < w \end{cases} \quad (11)$$

The width of the field free region is

$$a = \frac{w}{\cosh(B_a/B_f)} \quad (12)$$

with the characteristic field for the film geometry $B_f = \mu_0/\pi J_c$. The z -component of the magnetic field inside the thin film can be calculated from the current distribution with the Biot-Savart-law

$$B_z(x) = Ba + \frac{\mu_0}{2\pi} \int_{-w}^{+w} \frac{J_y(t)}{t-x} dt \quad (13)$$

and one obtains

$$B_z(x) = \begin{cases} 0 & |x| < a \\ B_f \ln\left(\frac{|x|\sqrt{w^2 - a^2} + w\sqrt{x^2 - a^2}}{a\sqrt{|x^2 - w^2|}}\right) & |x| > a \end{cases} \quad (14)$$

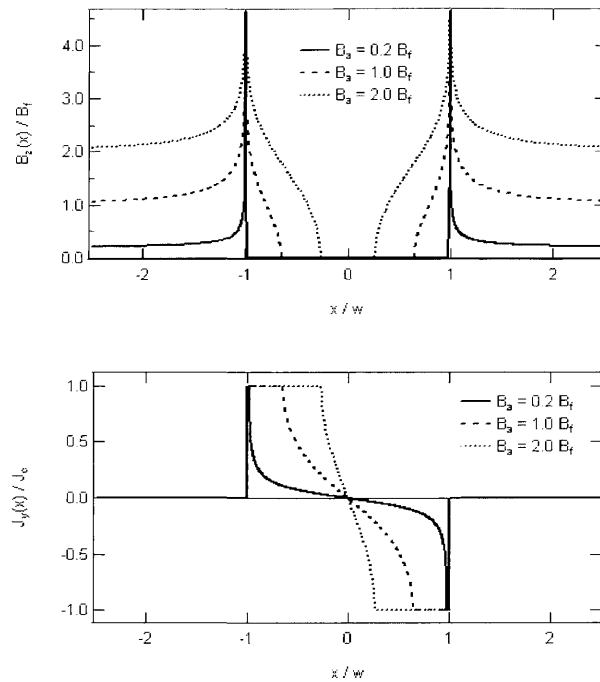


Figure 10: Field and current density distribution in a thin film in different applied fields B_a , calculated from the critical state model.

Those are the field and current distributions in a thin film with a perpendicular applied magnetic field. They are plotted in Fig. 10.

As in the Bean model for a slab geometry, the field inside a thin film depends on the magnetic history of the sample. A manifold of different cases can be calculated including alternating fields, application of a DC transport current in addition to a constant field, monotonically increasing field and current, etc. ([8], [9]). To describe the experiments in this work, the field distribution in a thin film with a constant perpendicular magnetic field B_a and an applied AC transport current $I(t)$ is needed.

This is done here in the following way:

1. Calculate the shielding current distribution from Eq. 11 without the transport current.
2. Calculate the current distribution for the transport current I_T and add it to the shielding current.

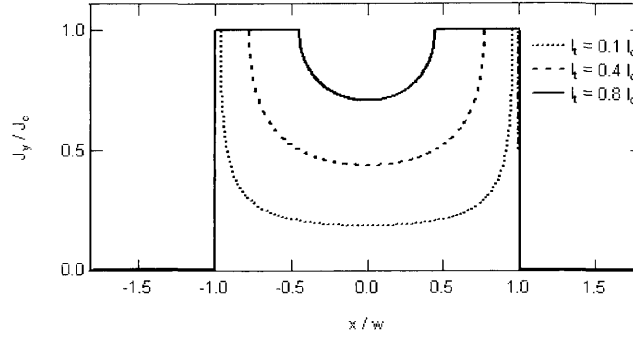


Figure 11: Current distribution in a thin film if only a transport current is applied.

3. Invert the sum of the two current distributions to obtain the B-field profile.

The current distribution in a film with only a transport current and *no* magnetic field applied can be calculated in a way similar to the case of an applied magnetic field. By conformal mapping one obtains

$$J_y(x) = \begin{cases} \frac{2J_c}{\pi} \arctan \left(\sqrt{\frac{w^2 - a^2}{a^2 - x^2}} \right), & |x| < a \\ J_c, & a \leq |x| < w \end{cases} \quad (15)$$

(16)

$$B_z(x) = \begin{cases} 0, & |x| \leq a \\ \text{sign}(x) B_f \ln \frac{\sqrt{w^2 - x^2}}{\sqrt{w^2 - a^2} - \sqrt{x^2 - a^2}}, & a < |x| < w \\ \text{sign}(x) B_f \ln \frac{\sqrt{x^2 - w^2}}{\sqrt{x^2 - a^2} - \sqrt{w^2 - a^2}}, & |x| > w \end{cases} \quad (17)$$

The width of the field free region $2a$ in this case is

$$a = w \sqrt{1 - (I_T / I_c)^2} \quad (18)$$

where I_c is the critical current corresponding to the full penetration of the strip. The current distribution in this case is plotted in Fig. 11.

However, this current distribution is subject to remanence effects, since the magnetic

field inside the sample is non-zero. It can not be applied in a straightforward way to the case of a time dependent current added to a shielding current. A current distribution that creates no magnetic field inside the strip is used here to represent the transport current. It can be calculated by conformal mapping of a constant current density flowing along the surface of a cylinder, which doesn't create a magnetic field on the inside, onto a thin film[9]. One obtains

$$J_y(x) = \frac{I}{\pi\sqrt{w^2 - x^2}} \quad (19)$$

where I is the magnitude of the applied transport current and w is the sample half width. It has to be noted, that this function apparently violates the constraint $J(x) \leq J_c$ imposed by the critical state model, since there are singularities at both edges $\pm w$. However, it has been successfully employed to interpret experimental data on thin films obtained by other groups[6], and also the results in this work can be interpreted reasonably well with this function.

To model the data, the transport current given by Eq. 19 [9] is added to the shielding current distribution (Eq. 11), and the resulting current profile is inverted to a B-field profile with the Biot-Savart law. Plots of the added current distribution and the resulting field distribution for different values of the applied current I_T relative to the critical current I_c are shown in Figs. 13, 14 and 15.

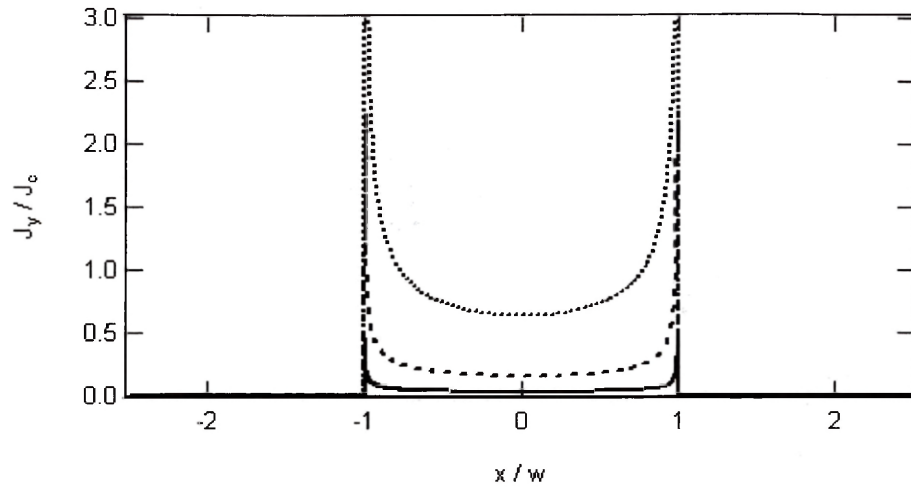


Figure 12: Plot of the transport current distribution according to Eq. 19, for different values of the applied current $I_T = 0.09I_c, 0.44I_c, 1.78I_c$.

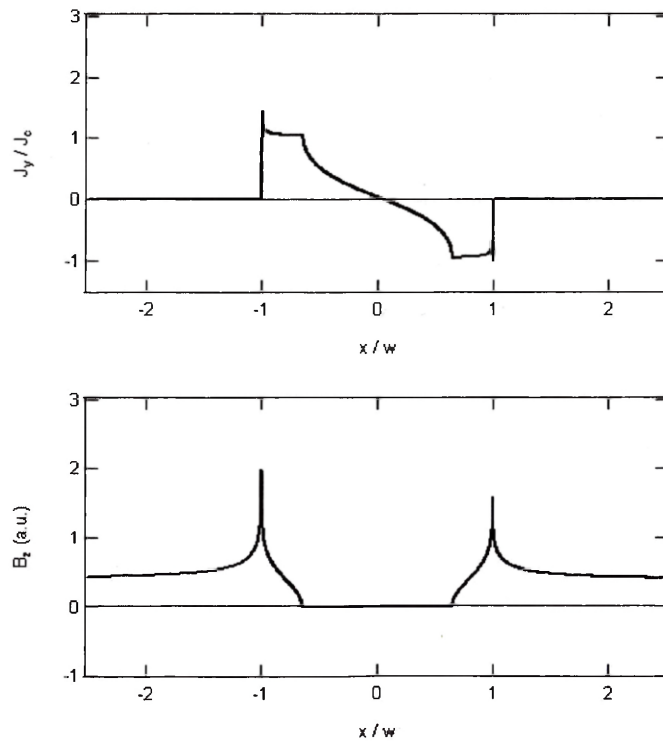


Figure 13: Current (top) and flux density (bottom) distribution in the case of an applied field and a *small* transport current $I_T = 0.09I_c$

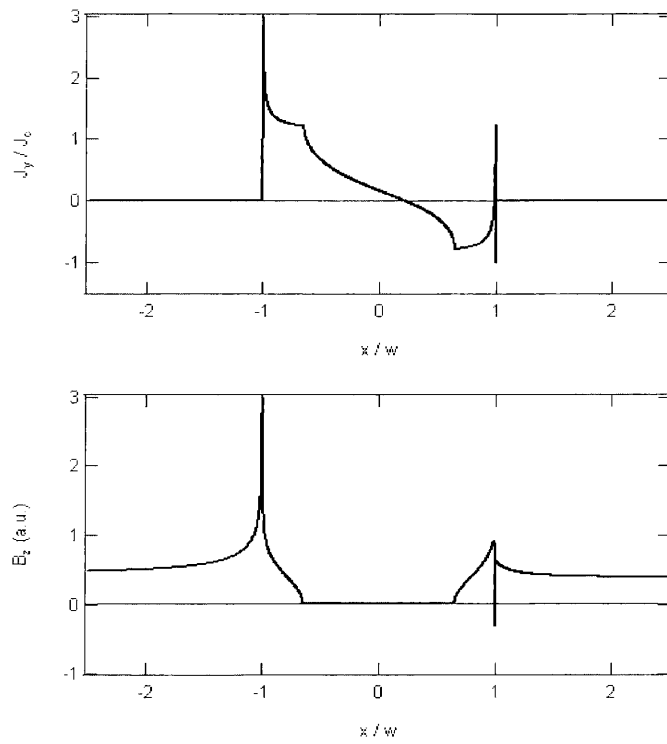


Figure 14: Current (top) and flux density (bottom) distribution in the case of an applied field and a *medium* transport current $I_T = 0.44I_c$

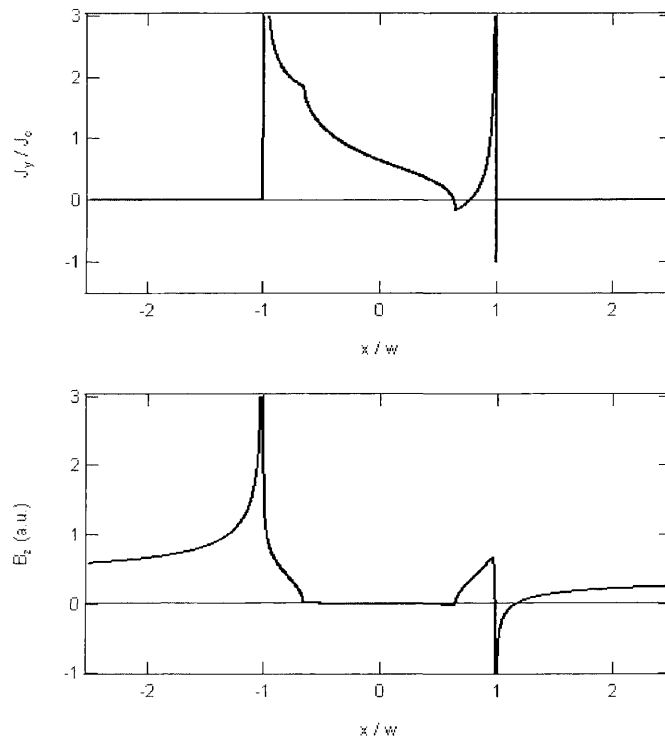


Figure 15: Current (top) and flux density (bottom) distribution in the case of an applied field and a *high* transport current $I_T = 1.78I_c$

3 Magneto-Optical Imaging (MOI)

3.1 Faraday Effect

To measure the two dimensional magnetic flux density distribution in a thin superconducting sample we utilize the magneto-optical Faraday effect in a thin film indicator which is placed on top of the sample. The Faraday effect describes the rotation of the polarization vector of linearly polarized light in certain materials, when an external magnetic field is applied parallel to the propagation direction of the light. The reason for this is an optical birefringence with the difference in real index of refraction between left and right circularly polarized light being proportional to the z -component of the local magnetization of the material[4].

The indicator film used for this work is a single crystalline iron garnet thin film with the composition $Bi_3(Fe, Ga)_5O_{12}$. It is ferrimagnetic with an in-plane magnetization M_s . If an external magnetic field H_z is applied perpendicularly, the magnetization is rotated out of plane by an angle

$$\phi = \arctan(H_z/H_k) \quad (20)$$

where H_k is the magnetic anisotropy of the film. The Faraday rotation angle Θ_F of polarized light incident perpendicularly on the indicator is proportional to the z -component of the magnetization and thus

$$\Theta_F = cM_s \sin(\phi) = cM_s \sin[\arctan(H_z/H_k)]. \quad (21)$$

The proportionality constant c contains also the distance the light travels in the indicator. By using a spatially resolved measurement of the rotation angle one can image the distribution of the perpendicular magnetic field in the indicator and also in the superconductor, because the indicator is kept close to the sample.

To record a two-dimensional magnetic flux density distribution, the spatial distribution of the Faraday rotation is measured with a polarization microscope and a digital camera.

Malus's law $I(\alpha) = I_0 \sin^2(\alpha)$ describes the light intensity I transmitted by a polarizer, if the incident light of intensity I_0 is polarized at an angle $\pi/2 + \alpha$ relative to the polarizer. The intensity transmitted by a pair of crossed polarizers in a polarizing microscope, with light polarization rotated in between them by the Faraday effect, is obtained by inserting equation 21 into Malus's law

$$I = I_0 \sin^2(\Theta_{I'}) = I_0 \sin^2(cM_s \sin[\arctan(H_z/H_k)]). \quad (22)$$

This idealized equation can be adapted to realistic conditions by introducing the background light intensity I' , which is transmitted by non-perfect polarizers in the cross polarized position, and by including a small deviation $\Delta\alpha$ of the polarizer and analyzer from the cross-polarized position:

$$I = I_0 \sin^2(cM_s \sin[\arctan(H_z/H_k) + \Delta\alpha]) + I'. \quad (23)$$

I_0 is the maximum light intensity that can be modulated with the Faraday effect, it includes any light absorption in the indicator and in both polarizers. The camera in the polarizing microscope records a two dimensional intensity distribution $I(x, y)$, and by inversion of equation 23 one obtains the magnetic flux density distribution from it:

$$B_z(x, y) = B_k \tan \left[\arcsin \left\{ \frac{1}{cM_s} \arcsin \left(\sqrt{\frac{I(x, y) - I'}{I_0}} + \Delta\alpha \right) \right\} \right]. \quad (24)$$

Fig. 16 shows the structure of the indicator. The indicator layer is grown epitaxially on a $Ga - Gd$ garnet substrate and has a thickness of $6\mu m$. There is a reflective layer (Al) below the indicator layer, so the polarized light passes the indicator layer twice. A protective layer is needed in order to avoid scratches of the indicator while mounting it on the superconductor. At an applied field, $H_z = 750Oe$, the indicator shows a Faraday rotation of $1.08deg/\mu m$.

The spatial resolution of the magnetic field images measured with magneto-optical

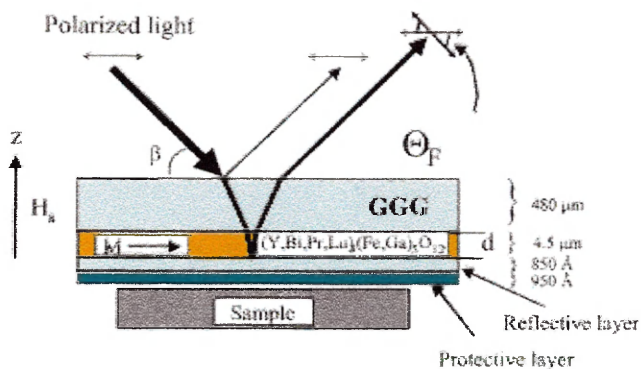


Figure 16: The ferrite-garnet based magneto-optical indicator. The polarization direction of light passing through the indicator layer is rotated by an angle Θ_F proportional to the local perpendicular magnetic field.

imaging (MOI) depends strongly on the distance between the indicator and the sample. If the distance is large the resolution and contrast of the image decreases. The ideal case would be an indicator film that is grown directly on the sample. However, this is not an option for the indicator material used here, since a very low defect density is required and $Ga - Gd$ garnet is needed as a substrate.

In an ideal indicator the spontaneous magnetization is perfectly in-plane and is homogeneous throughout the film. In reality, however, there can be magnetic domains in the indicator where the Faraday response is different, which are seen as differently shaded regions in the magneto-optical images. The Bloch walls around those regions are seen as jumps in the image intensity, which can be as high as 30% of the intensity. By averaging the intensity over a large region, as done in the experiment by taking line profiles over a certain width, the effect of such local jumps can be minimized.

An alternative technique to obtain magnetic field images would be, for example, to scan the sample surface with a micro Hall probe. This generally provides a higher resolution (submicron [15]) and also has the advantage that the magnetic field is measured directly. However, as the focus of this work is the study of time dependent evolution of magnetic field distributions, a scanning technique with serial data acquisition can not provide the high acquisition speed required for this work. In magneto-optical imaging data is recorded

in parallel by taking images with a pulsed laser and a digital camera, which in our case can be as fast as a 100 nanoseconds.

Another method would be, to place a one- or two dimensional array of micro Hall probes on the sample surface, which could be read out simultaneously and would provide good time resolution capabilities. A drawback here is the low spatial resolution of such arrays, which is generally worse than what can be achieved with magneto-optical imaging[16].

3.2 Experimental Setup

The general experimental setup for magneto-optical imaging of superconductors consists of a polarizing microscope, imaging equipment such as a CCD camera, an optical cryostat that holds the sample with the magneto-optical indicator on top of it, as well as an electromagnet to apply a field perpendicular to the sample surface, as shown schematically in Fig. 17.

The objective of this thesis is to obtain time-resolved images of the field distribution in superconductors with an AC current applied. This requires first a current source and second a method to synchronize image recording with the phase of the transport current. In this work, synchronization is achieved by stroboscopic illumination of the indicator with nanosecond pulses of polarized laser light. The pulses are emitted at certain, exactly controllable phase points of the alternating current and between them no light reaches the indicator (Fig. 17). The exposure time of an image taken with the camera now is much longer than the period of the AC current, so that one image contains the average over many laser pulses. But since no light reaches the indicator or the camera between pulses, an image contains information of the magnetic field distribution only at the observed phase point.

In the following, the individual components of the setup are presented.

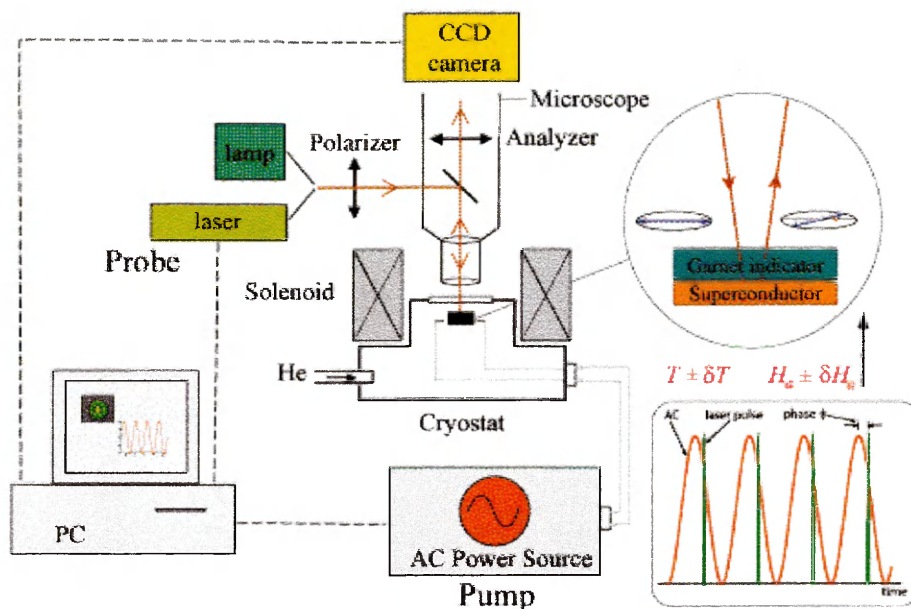


Figure 17: MOI setup. As light sources a Hg-vapor lamp and a pulsed laser are available, but only the laser can be synchronized to the AC current source in order to take stroboscopic time dependent measurements.

3.2.1 Imaging Equipment

Light Source — A diode-pumped, frequency doubled Nd:YLF laser with a wavelength $\lambda = 527nm$ is used as the light source. Laser pulses with a width of $\tau = 100ns$ are generated by Pockels Cell (q-switch). In the experiment, the laser pulse repetition frequency (PRF) is varied between 100 – 1000Hz, according to the frequency of the AC current. It is synchronized with the phase of the current with a synchronization circuit described in section 3.2.2.

The laser light is coupled into an optical fiber and is transferred to the microscope where it is expanded via a set of lenses which forms a telescope. This telescope was built in order to optimize the coupling of the laser light into the microscope and to obtain a homogeneous intensity distribution in the recorded images. The coherent light from the laser requires anti-reflection coatings on some of the optical components of the microscope (such as beamsplitter, windows,...), in order to avoid interference effects.

A Hg vapor lamp is also available in the microscope, but it can only be used to

take static magneto-optic images since it can not be synchronized to the AC current. However, the Hg lamp has the advantage over the laser that its light is not coherent, and thus interference effects do not occur.

Microscope — The polarizing microscope has been custom assembled with components from Olympus. It is equipped with a Glan-Thompson polarizer and a linear polarizer, providing an extinction ratio of about 10^{-5} . The angle of the analyzer relative to the polarizer can be adjusted manually. The microscope can hold fluorite tension-free objectives with magnification ranging from 4x to 20x, which minimize depolarization effects. For this work only the 4x objective has been employed in order to have a large field of view. Additionally, the resolution of the magneto-optical images is more limited by the distance between the indicator and the sample than by the magnification of the microscope.

Camera — A Hamamatsu ORCA-ER-1394 CCD camera is mounted onto the microscope to record images. The camera has a resolution of 1344×1024 pixels and the CCD is peltier cooled to achieve a low dark noise with a dynamic range of 2000 : 1. The exposure time can be in the range $10\mu s \leq \tau \leq 4600s$. In the experiment, the exposure time is varied in the range $20ms \leq \tau \leq 700ms$, depending on the frequency of the AC current and thus on the number of light pulses hitting the chip per second. The recorded images are transferred to a PC for storage and processing.

In order to enhance the field of view, a demagnifying adapter with a demagnification of $0.63\times$ has been mounted between the camera and the microscope. By spatial calibration the real length corresponding to one pixel of an image has been determined to be $2.494\mu m$. The resulting field of view is then $3.35mm \times 2.55mm$.

The spatial resolution in this work is estimated on the basis of the number of pixels. The smallest appreciable feature has to have at least the size of two to three pixels, giving a resolution of about $5\mu m$ to $7.5\mu m$.

The spectral sensitivity of the camera has its maximum at the wavelength $\lambda = 527nm$

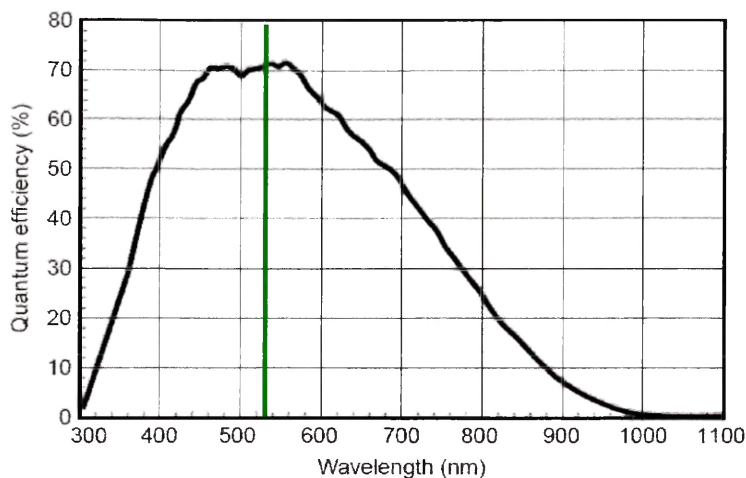


Figure 18: Spectral sensitivity of the camera. The wavelength of the laser is $\lambda = 527nm$.

of the laser light, as shown in Fig. 18.

Cryostat and Sample Holder — The sample and the indicator are placed inside a continuous-flow cryostat which is cooled with liquid helium. In order to cool YBCO samples below their critical temperature of $91K$, cooling with liquid nitrogen would be sufficient. However, at liquid nitrogen temperature the magnetic flux lines can penetrate further into the sample and the overall magnetic flux profile is much more homogeneous, resulting in low contrast of the recorded images. The temperature range of the cryostat is $3.5K$ to $325K$, measurements were done at $T \approx 24K$.

The sample is mounted on top of a custom-made copper sample holder, which in turn is fixed on top of the coldfinger of the cryostat. A small quantity of silver paint is applied on the bottom of the sample to ensure good thermal conductivity. The indicator crystal is placed on top of the sample and is fixed to the sample holder by two aluminum strips. Two strips of copper-beryllium provide electrical contact to the sample, which are mounted on a teflon substrate in order to insulate them from the copper sample holder. Copper-Beryllium is selected as contacting material because it offers a good electrical conductivity of about 22% of that of annealed copper but a higher mechanical strength, so that good contact is achieved when the sample is cooled down.

The sample holder also incorporates a thermal sensor and a Hall sensor. The Hall sensor is placed about four millimeters below the sample in the center of the sample holder and measures the magnetic field along the z-direction perpendicular to the sample surface. The distance between the sample and the position of the Hall sensor causes a slight difference between the measured field and the field that is present in the sample plane. The measured B-field values are corrected for this effect.

Magnet — An electromagnet which can deliver magnetic fields parallel to the z-axis from -65mT to 65mT is mounted on top of the cryostat. The sample is placed accurately in the center of the solenoid, in order to avoid stray fields along the x and y direction, which would influence the in plane magnetization of the indicator film and would reduce the response for an applied field along the z-direction.

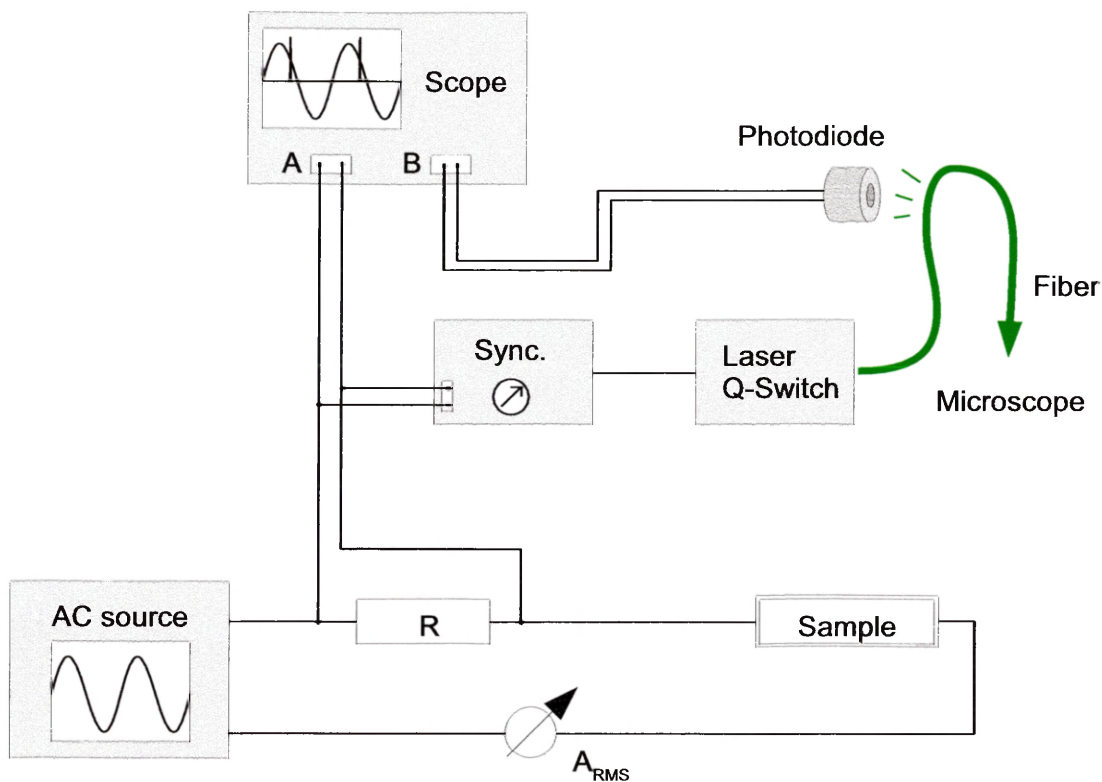


Figure 19: Block diagram of the synchronization scheme. The phase of the AC current at which laser pulses are triggered is adjusted with a home-built synchronization circuit. The laser pulses are detected with a photodiode and are displayed on an oscilloscope together with the transport current signal, in order to control the relative phase.

3.2.2 Synchronization

An electronic circuit that synchronizes the laser pulses with the AC current has been designed and built up as part of this work. The synchronization scheme is shown in Fig. 19.

The current source can deliver AC currents of customizable waveform with an amplitude of up to 15A. The current is sent through a load resistor $R = 3.8\Omega$ with the sample in series and is controlled by a separate multimeter. The AC signal is picked up from the load resistor, displayed on an oscilloscope and sent to the synchronization circuit as input. The synchronization circuit then sends a trigger pulse to the laser with a finely controllable time delay Δt with respect to the phase $\phi = \omega\Delta t$ of the current signal. The generated laser pulses are then sensed by a photodiode and displayed on the oscilloscope

together with the AC signal, in order to precisely determine ϕ .

A detailed schematic of the synchronization circuit can be found in the appendix. The circuit is based on the timer chip IC 555, which, in monostable operation mode, generates a pulse with a time delay after an incoming trigger signal based on the discharge time of a capacitor. By varying the resistance of a potentiometer in series with the capacitor, the discharge time and thus the time delay can be controlled. The time delay is given by $\Delta t = 1.1RC$, where R is the resistance of the potentiometer and C is the capacitance.

The circuit consists of two delay stages in series: one that is finely controllable and a second, more coarse one, that adds another delay to the first one in order to overcome the intrinsic limitation of the IC 555 chip that it can only cover 95% of the duty cycle. By adding another delay with a second timer chip it is possible to get $\phi \geq 2\pi$. This is needed in order to take images over the whole AC current cycle and also to assure that images taken at $\phi = 2\pi + \epsilon$ are consistent with those taken at $\phi = \epsilon$.

The output signal of the circuit is amplified by an SRS voltage amplifier before being sent to the laser Q-switch.

3.3 Calibration

For quantitative magneto-optical measurements, the system of light source, indicator, and camera has to be calibrated. The calibration has been done immediately before the experiment, with the sample and the indicator mounted in their respective position for the experiment. A series of magneto-optical images is taken with the applied B-field increased from $B_a = 0mT$ to $65mT$ in steps of about $2mT$. In each image, the average intensity in an area far away from the sample is calculated, and it is plotted against the magnetic field to get the calibration curve.

One calibration image taken at $65mT$ is shown in Fig. 20 and the area where the intensity is extracted is marked at the top and the bottom of the image (the region of interest). The calibration curve is shown in Fig. 21. A laser pulse repetition frequency of $1kHz$ and an exposure time of $20ms$ have been used for calibration. Since the Faraday

effect is slightly temperature-dependent, the calibration has been done at about the same temperature as in the actual experiments ($T = 18k$).

The calibration parameters determined by fitting equation 24 to the data points in Fig. 21 are

$$\begin{array}{ccccc} B_k & CM_s & I_0 & \Delta\alpha & I' \\ \hline 175.43 & 2.1115 & 328.5 & 0.0096597 & 14.35 \end{array}$$

The influence of the sample on images used to calibrate the imaging system is not wanted. However, the alternative of calibrating the system in a separate run after taking data would require to heat up the system, to remove the indicator and the sample, and to mount the indicator again. This procedure has been found to have an influence on the parameters I' , I_0 and $\Delta\alpha$, which have to be known exactly for quantitative magneto-optical imaging. Calibration images are thus taken with the sample in place, and the region of interest is chosen sufficiently far away from the sample in order to minimize its influence.

The image intensity depends on the magneto-optical effect, but also on the number of laser pulses hitting the CCD chip during one exposure time period. Before being calibrated, the intensity of an image taken at a certain exposure time and frequency has to be converted to match the number of pulses per exposure time of the images used for recording the calibration curve. The light intensity of an image approximately has a linear relation with exposure time and frequency

$$I = f * \tau * sig + B \tag{25}$$

where I is the image intensity, f is the frequency, τ is the exposure time and sig is the intensity of one Faraday rotated laser pulse as it is registered by the camera. One would expect the intensity to be zero if no light pulse hits the camera, but experimentally a background intensity B is observed, which is attributed to a constant noise in the camera. If B is determined, an image can be converted from one set of frequency and exposure

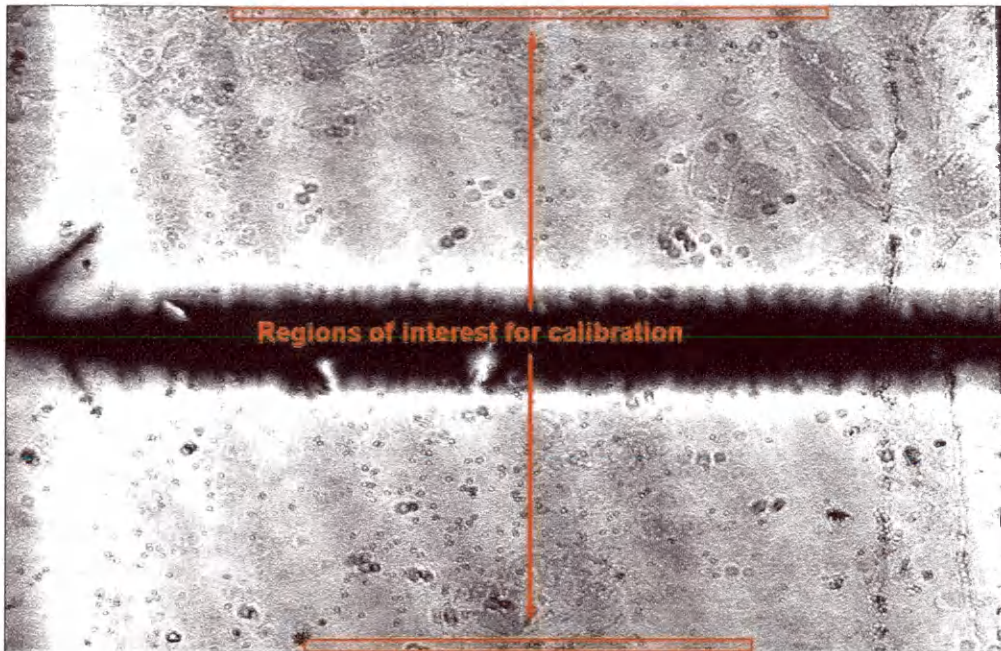


Figure 20: Magneto-optical image used for calibration. The field on this image is $B = 65mT$.

time to another with the relation

$$I_2 = \frac{f_2\tau_2}{f_1\tau_1}(I_1 - B) + B \quad (26)$$

3.4 Samples

The samples studied in this work are multilayered $YBa_2Cu_3O_{7-\delta} / Y_2BaCuO_5$ thin films grown by pulsed laser deposition. The $YBa_2Cu_3O_{7-\delta}$ are complete layers with 6nm to 15nm thickness, in between two such layers there is one layer of isolated, disk shaped Y_2BaCuO_5 nano-particles with a height of 1nm to 2nm. The Y_2BaCuO_5 nano-particles are included in order to strongly enhance flux pinning. The area density of these particles is estimated $\approx 10^{11}cm^{-2}$, which theoretically allows them to pin a flux density of $B \approx 2T$ (assuming that one disk can pin one flux line containing a flux $\Phi = 2.07 \times 10^{-11}T \cdot cm^2$). The thickness of the sample is not precisely known, it lies between 250nm and 350nm.

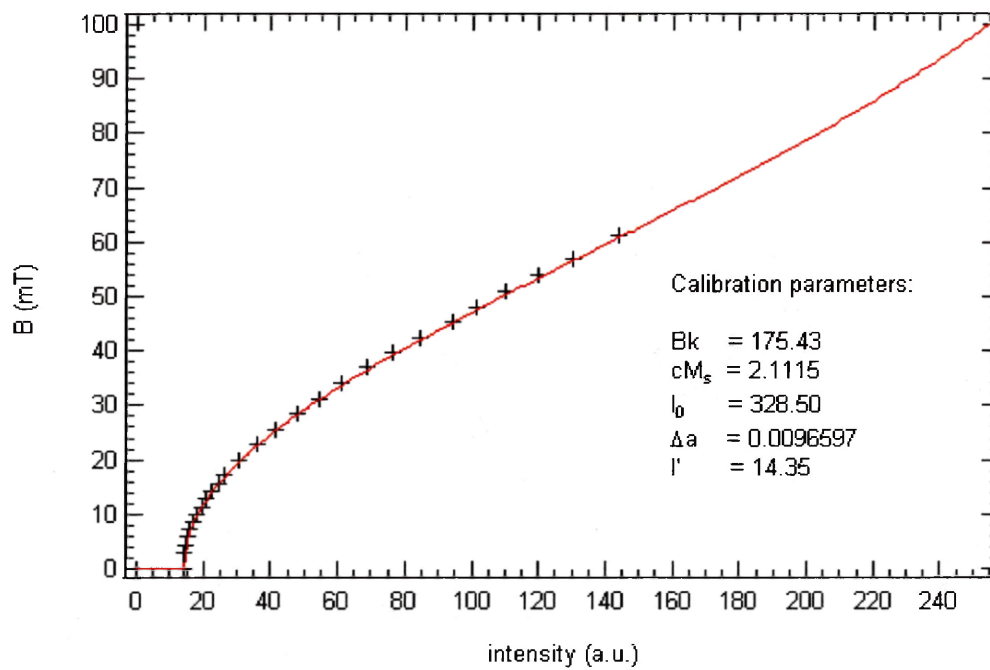


Figure 21: Calibration curve for quantitative magneto-optical measurements. The temperature is $T = 18K$, the laser prf is $1000Hz$, and the exposure time of the camera is $\tau = 20ms$.

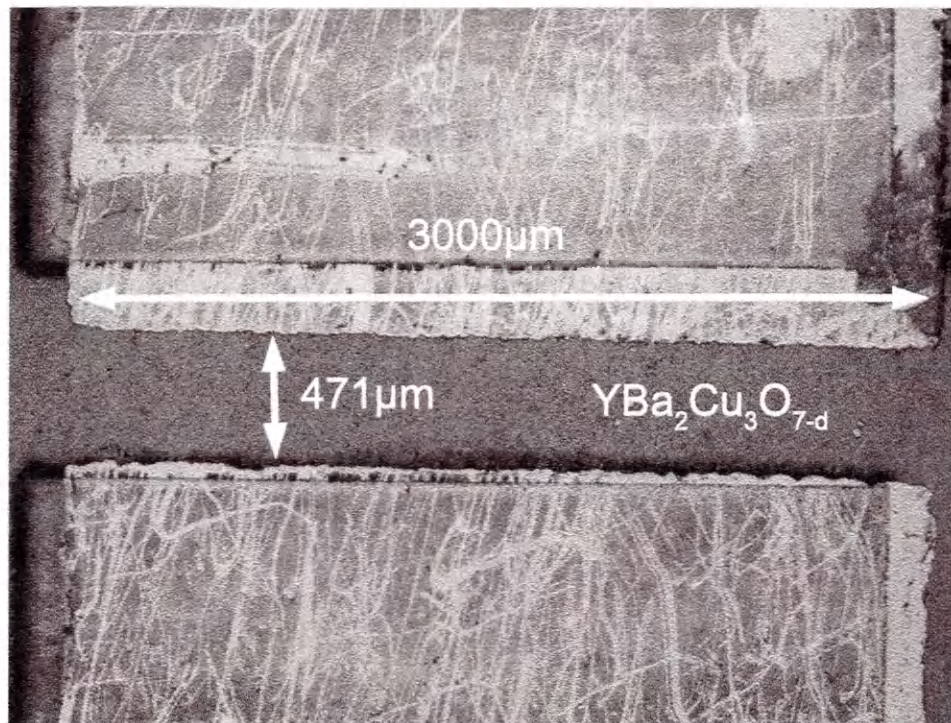


Figure 22: Optical micrograph of a YBCO sample.

The films are grown on a $LaAlO_3$ substrate, the overall size of the samples with the substrate is roughly $10\text{mm} \times 5\text{mm}$. The sample is bridged using a photolithographic technique, in order to decrease the critical current. The bridge length is 3mm and the width $2w = 471\mu\text{m}$. An optical micrograph of the sample is shown in Fig. 22.

A critical temperature of $T_c = 91\text{K}$ has been determined from AC susceptibility measurements. A plot of the DC resistance versus temperature is shown in Fig. 23. Transport measurements at 77K show a critical current density $J_c(77\text{K}) = 1.5 \times 10^6 \text{A/cm}^2$, an extrapolation of the temperature dependence of J_c to $T = 10\text{K}$ yields $J_c(10\text{K}) = 55 \times 10^6 \text{A/cm}^2$.

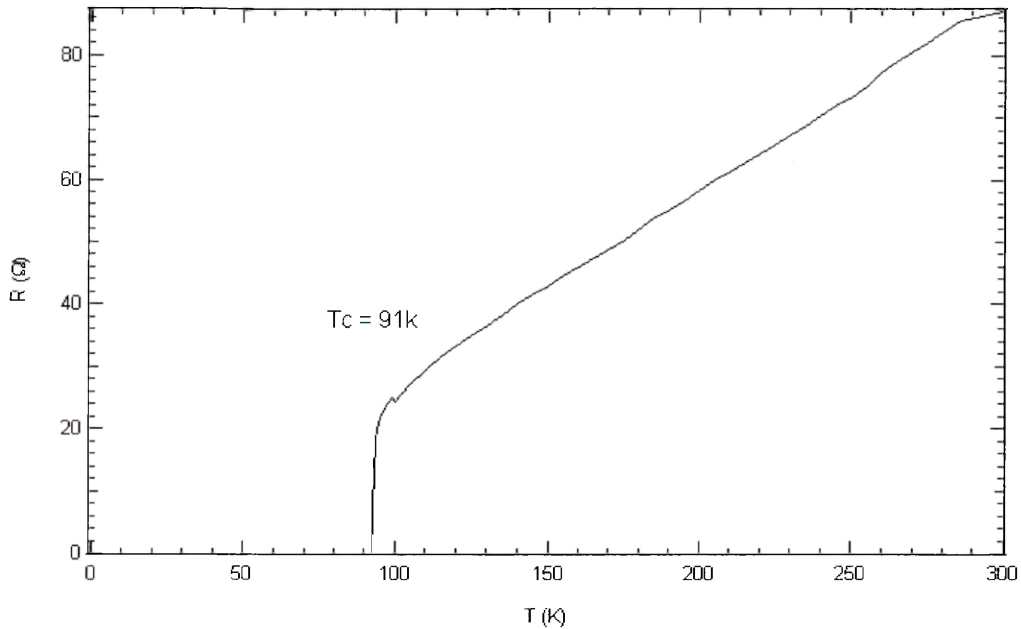


Figure 23: DC resistance versus temperature curve for a YBCO thin film sample.

4 Frequency Dependent Measurements

The magnetic field distribution in the sample with an applied AC current has been measured at different frequencies of the applied current, in order to determine if time dependent magnetic effects, such as thermally activated flux creep, lead to a frequency dependence in the magnetic field distribution.

The sample is zero field cooled to $T = 24K$. When the sample has reached the temperature, a perpendicular magnetic field $B_a = 10mT$ is applied and an AC transport current with sine waveform and amplitude $I_{max} = 8.54A$ is sent through the sample. The frequency is varied in the range $f = 100Hz \dots 1000Hz$ with a stepsize of $100Hz$. The exposure time for the images has been chosen so that at each frequency the images contain information at one phase point averaged over 20 to 50 cycles of the current. At each frequency five magneto-optical images are taken: one each at the maximum, minimum and the zero phase point of the current, and one each between the maximum and zero and between zero and the minimum.

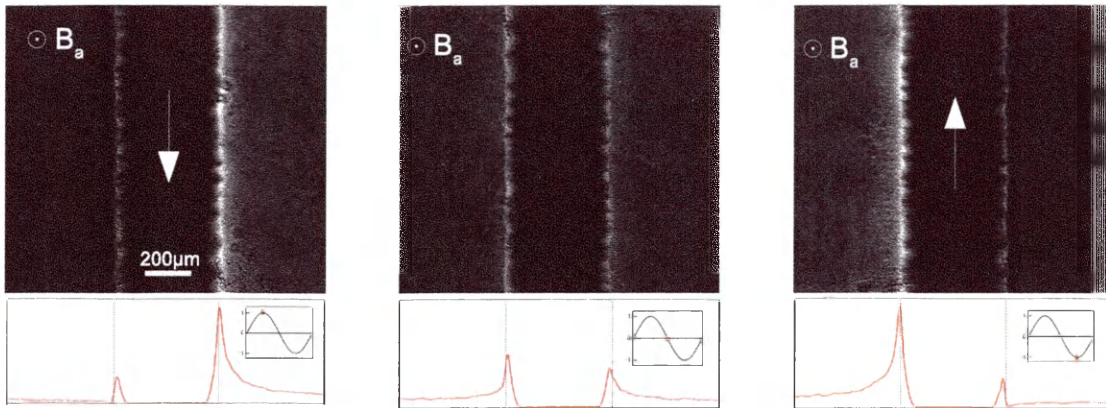


Figure 24: Magneto-optical images of the bridge at $f = 1000\text{Hz}$, taken at the maximum, zero and minimum phase points of the AC current. The intensity profiles obtained by averaging parallel to the bridge are shown below the images.

As an example, the images recorded at $f = 1000\text{Hz}$ are shown in Fig. 24. Due to the Meissner effect the magnetic field is expelled from the sample center, and the images are dark in that region because there is no Faraday rotation. Due to demagnetization the flux density is increased at the sample edges, and the edges are seen as bright areas in the images. The influence of the transport current can clearly be seen in the change of intensity at the left and the right edge, when the images at maximum and minimum current are compared. At the zero point of the current, the intensity at both edges is approximately equal.

For further quantitative analysis the intensity is averaged parallel to the bridge to give one dimensional profiles. In the profiles, the effect of local defects in the indicator is mostly averaged out. Fig. 24 shows only a part of the recorded images with emphasis on the sample. The full images extend laterally over about six times the sample width, which is an advantage for the accurate inversion of a calibrated intensity profile to obtain the current distribution in the sample.

The profiles recorded at different frequencies and image exposure times are not directly comparable in intensity values because the number of laser pulses contributing to one image is different. The intensity profiles are thus corrected as described in section 3.3. Fig. 25 shows a plot of the image intensity as a function of the number of light pulses,

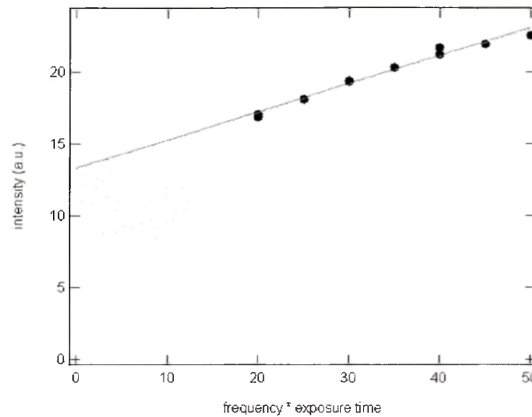


Figure 25: Intensity of MOI images versus the number of collected light pulses, which is given by the product of current frequency and exposure time. A y-axis offset $B = 13.8 \pm 1.4$ is obtained from a linear fit, it is needed as a parameter in the exposure time correction with equation 26.

which has been obtained from the set of frequency dependent images at the zero phase point of the current. It is used to determine the parameter B for the exposure time correction. The behavior is linear in good approximation with a background intensity $B \neq 0$, which justifies the phenomenologic equation 25. By extrapolation to $f\tau = 0$ one finds a mean offset

$$B \approx 13.8 \pm 1.4 \quad (27)$$

from three such plots at the three phase points. Using equation 26, one can then convert the intensity profiles recorded at different frequencies to the frequency $f = 1000\text{Hz}$ and exposure time $\tau = 20\text{ms}$ that has been used for the calibration.

The converted intensity profiles at the three phase points are shown in Figs. 26 – 28. A detailed discussion of the shape of the profiles and the behavior with the phase of the current is given in section 5, the focus of this section is only on frequency dependent effects.

Figs. 26 – 28 show that there is a small difference in the intensity between profiles at different frequencies. As can be seen in the insets of Fig. 26, there is a spread of about 13 intensity units ($\approx 16\%$) in the peak height at maximum transport current on the right sample edge, with the curve at 300Hz being the highest and 1000Hz being the

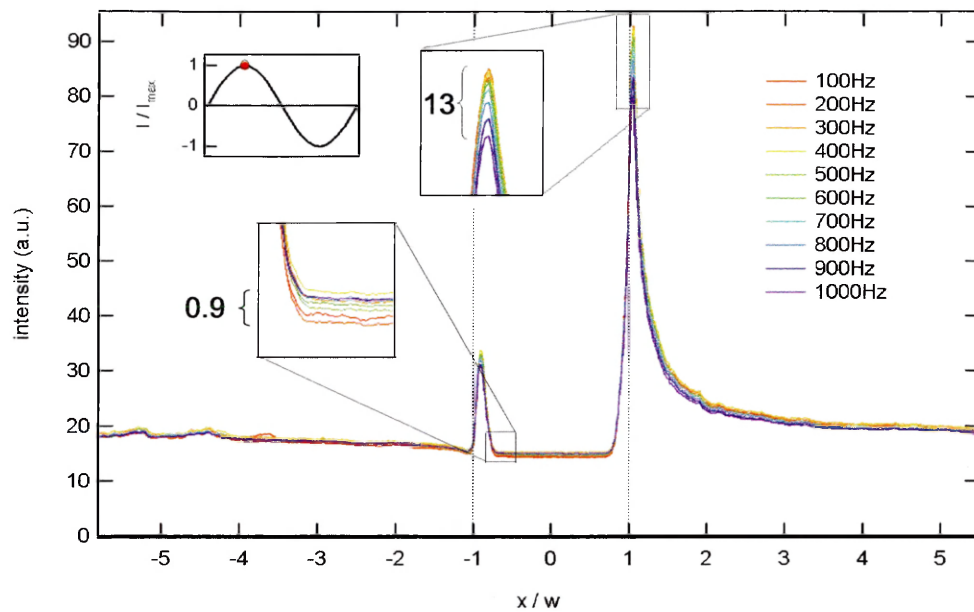


Figure 26: Frequency dependent intensity profiles at maximum AC current. The broken lines mark the edges of the sample.

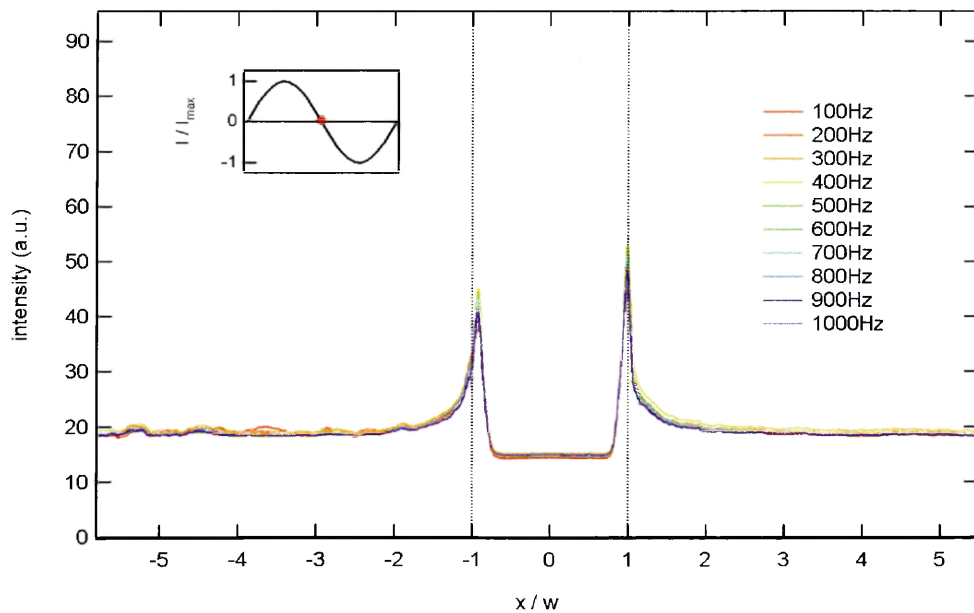


Figure 27: Frequency dependent intensity profiles at zero phase point of the AC current. The broken lines mark the edges of the sample.

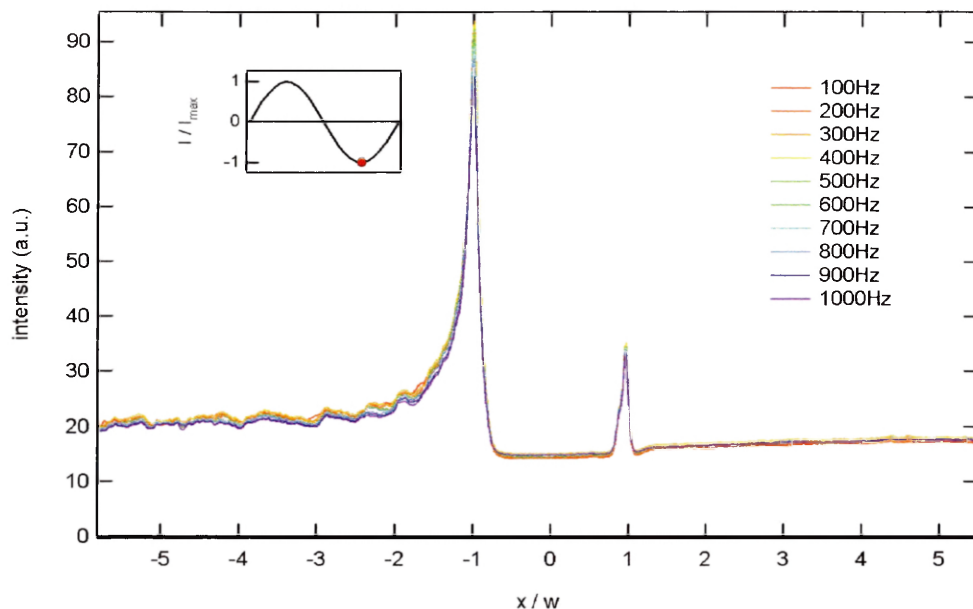


Figure 28: Intensity profiles across the bridge for different frequencies at the minimum of the transport current.

lowest. In the sample center the intensity values are spread by ≈ 0.9 corresponding to 6%, with $400Hz$ having the highest intensity and $200Hz$ having the lowest. This difference is consistent on all three phase points. However, there is no clear trend with the frequency, and the positions of important features, such as the flux penetration front and the peaks are constant within about ± 2 pixels. Furthermore, the intensity should be the same for all frequencies at positions where there is clearly no magnetic field, such as in the sample center.

The observed effect is thus considered to be an artifact due to the imperfect exposure time correction, with an error in the parameter B of about 10% [27]. To eliminate this artifact the intensity profiles are normalized according to the relation $y' = Xy + Z$, where the parameters X and Y are chosen such that the frequency dependent profiles at one phase point (minimum phase) overlap with the profile at $f = 1000Hz$ on two different points (points of lowest and highest intensity). The same normalization parameters are used to transform the profiles at all three phase points at one frequency.

The normalized profiles are shown in Figs. 29 – 31. For completeness, the normalized

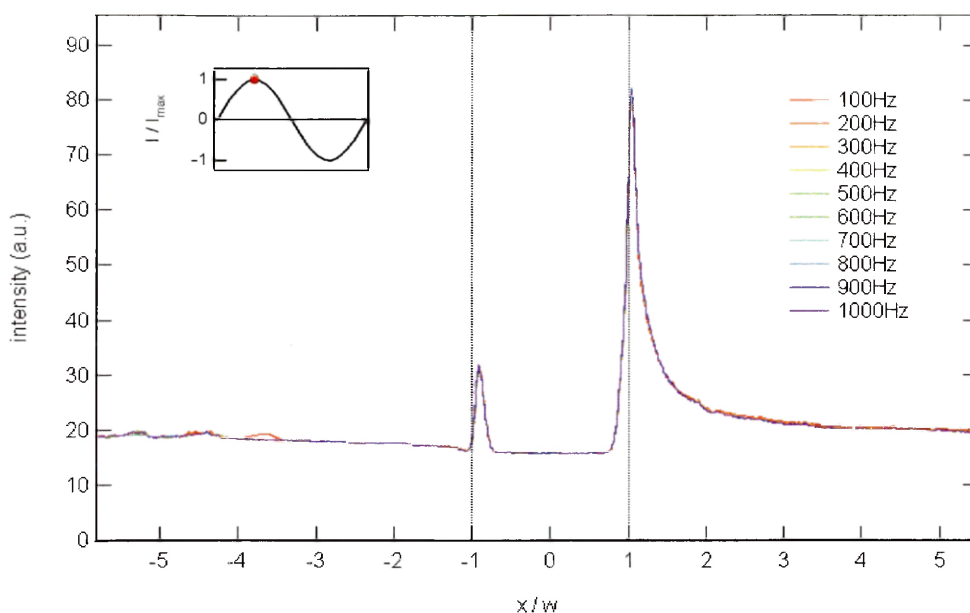


Figure 29: Normalized intensity profiles for different frequencies at maximum transport current.

profiles have also been calibrated (section 3.3) and the resulting B-field distributions are shown in Figs. 32 – 34.

It can clearly be seen that the normalized frequency dependent magnetic flux distributions at all three phase points overlap strikingly well. The regions where there is some deviation from perfect overlap, as on the rough parts on the left side of the profiles, can be attributed to defects in the indicator which have not been completely averaged out. In a defect the indicator’s response to a magnetic field is different than in the rest, and the exposure time correction as well as the calibration with the parameters used for the intact parts of the indicator do not apply exactly.

From these results it can be concluded that there is no appreciable frequency dependent effect in the magnetic behavior of the superconductor, for AC currents in the frequency range of $100Hz \leq f \leq 1000Hz$. Flux jumps and thermally activated relaxation apparently do not have an influence on the frequency behavior in this low current and low temperature regime.

At temperatures closer to T_c , thermal activation of flux motion is more likely and flux

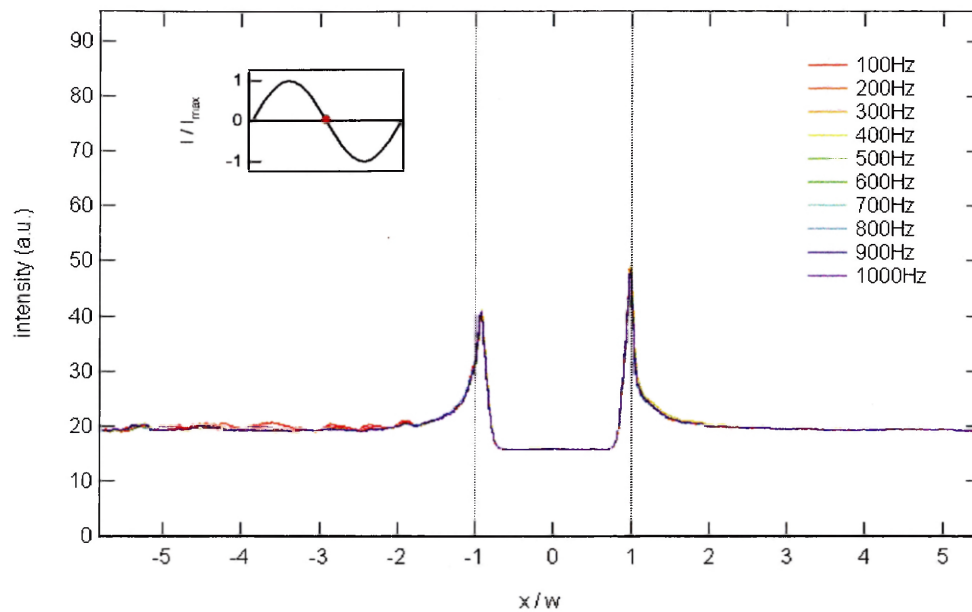


Figure 30: Normalized intensity profiles for different frequencies at the zero phase point of the transport current.

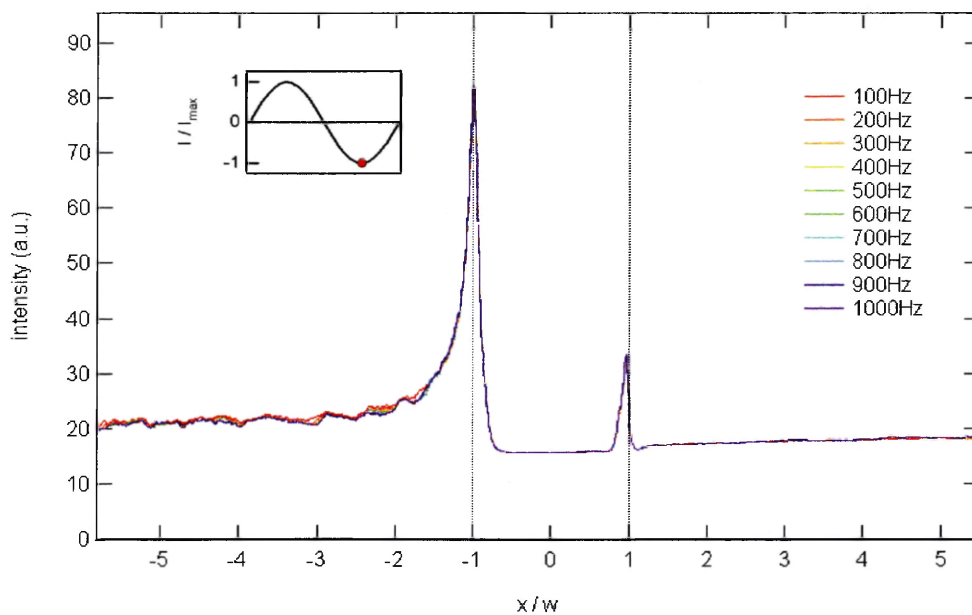


Figure 31: Normalized intensity profiles for different frequencies at the minimum of the transport current.

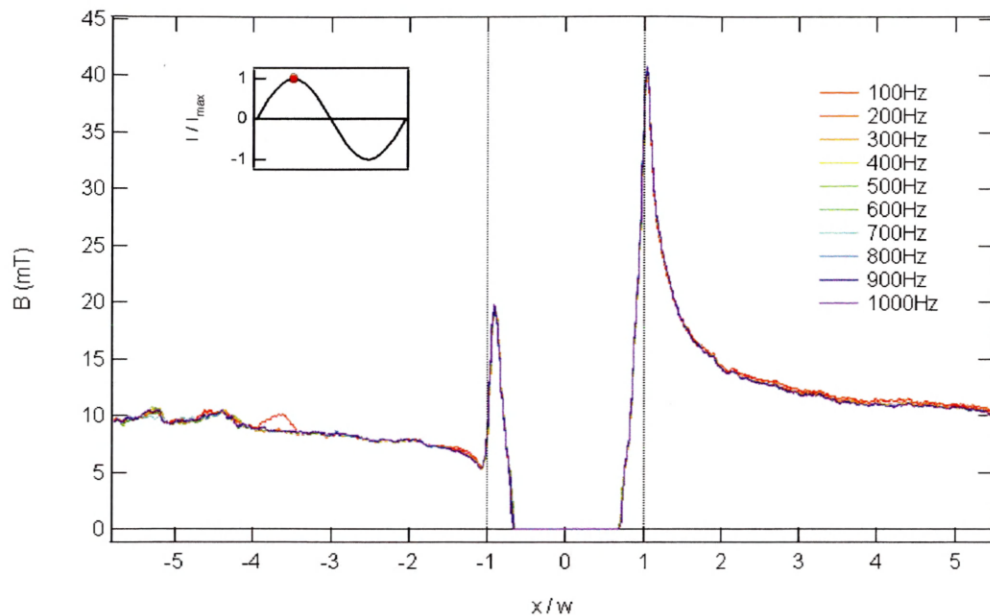


Figure 32: Magnetic flux density profiles across the bridge for different frequencies at maximum transport current. The flux density has been manually set to $B = 0mT$ in the sample center.

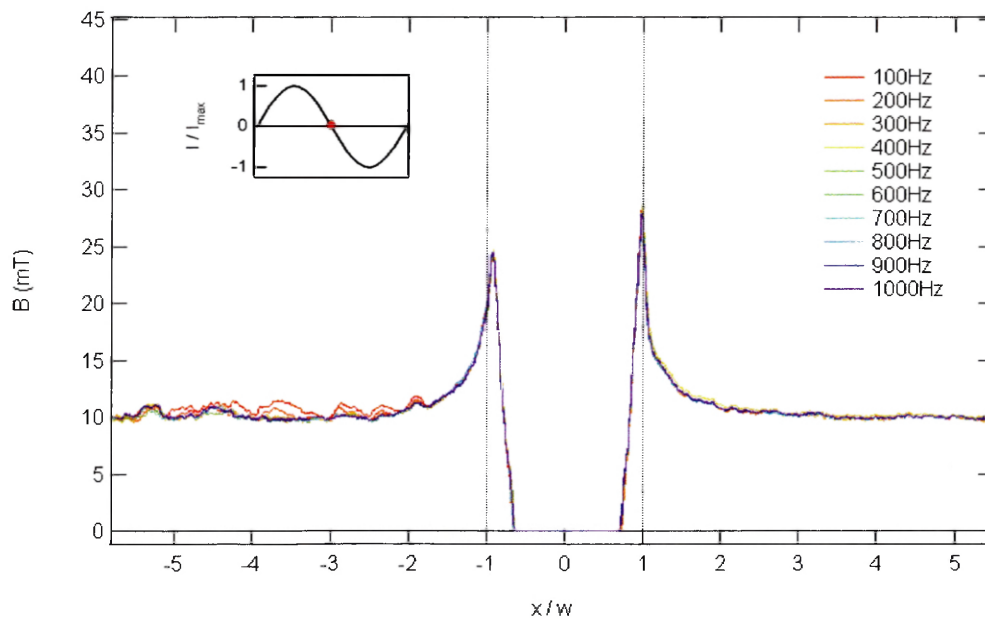


Figure 33: Magnetic flux density profiles across the bridge for different frequencies at the zero phase point of the transport current. The flux density has been manually set to $B = 0mT$ in the sample center.

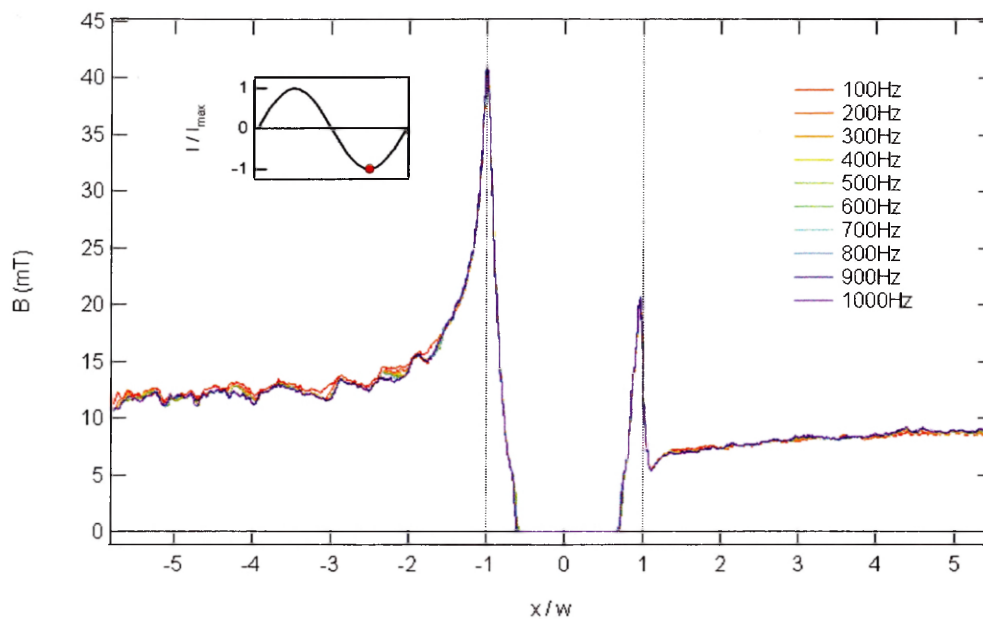


Figure 34: Magnetic flux density profiles across the bridge for different frequencies at the minimum of the transport current. The flux density has been manually set to $B = 0\text{mT}$ in the sample center.

creep might play a greater role especially at low current frequency, where the B-field is varying slowly. At higher B-fields, the probability of flux jumps during the current period increases and those might introduce a frequency dependence of the profiles.

5 Phase Dependent Measurements

MO images are taken at 25 equidistant phase angles over one current period at $1000Hz$. As in the frequency dependent measurements, the amplitude of the applied sine current is $I_{max} = 8.54A$ and a perpendicular magnetic field $B_u = 10mT$ is applied. The sample has been cooled in zero field to a temperature $T = 22K$. The exposure time of one image is 50ms, it thus contains information of one phase point averaged over 50 cycles of the current. Intensity line profiles over the sample cross section are taken from the images, and they are processed and calibrated in the same way as in the frequency dependent measurements.

Magnetic Field — The resulting magnetic field profiles over the first and second half wave of the current are shown in Figs. 35 and 36, the same profiles with focus on the important peak structure are shown in Fig. 37.

As seen in Figs. 35 and 36 the magnetic field approaches the applied field of $10mT$ far outside the sample, which is an indication that the calibration is quantitatively correct. The wiggles in the range $x < -2.5w$ and at $x \approx +2w$ are artifacts which are attributed to Bloch walls in the indicator. By comparing Figs. 35 and 36 one finds that B-profiles corresponding to the same transport current in the decreasing and increasing current half wave are identical. This is an indication that remanence effects can be neglected in these measurements. Also, profiles at phase angles where the transport currents are equal in magnitude but have opposite direction are found to be symmetric to each other.

The field peaks at the sample edges change about $19mT$ in height as the current changes from maximum to minimum, and they move from immediately outside the sample edge to about $14\mu m$ inside the sample. At the current extrema, a dip in the magnetic field forms outside one of the sample edges at $|x| \approx 1.06w$. The magnetic field inside the sample has an approximately linear gradient of $\frac{\partial B}{\partial x} \approx 117.5T/m$, it reaches zero at the flux penetration front at $a = (0.73 \pm 0.01)w$.

Within the region $|x| < a$ the magnetic field has been set to 0mT manually. The

reason for this measure is that the calibration function (Eq. 24) strongly amplifies noise in the intensity at low intensity levels $I \approx I(0mT)$, due to the vertical gradient $\partial B/\partial I$ (if $\Delta\alpha \approx 0$). A small level of noise in the recorded images in the sample center results in oscillations of several mT around $B = 0mT$. The B-field profiles are thus set to 0mT in the sample center region. The kink in the B-field profile originating from this measure at the edges of the center region has been removed by smoothing.

The transport current has only little influence on the magnetic field inside the sample, apart from the movement of the peak. The field in the linear range increases by roughly $1.7mT$ as the adjacent peak increases from minimum to maximum in one half period of the current. The flux penetration front is estimated to vary by less than $4\mu m$, which is within the stated spatial uncertainty of the measurement. An important result at this point is that flux jumps are not observed at any point of the phase of the AC current. A jump would be observed, if in the transition from one phase point to the next the flux density inside the sample would increase significantly.

If the flux density profiles at all phase points are integrated, one obtains the total magnetic flux through the region of an image. This flux should be independent of the transport current, since flux lines are only expelled from the sample and are not generated or destroyed, and the self field of the current should give no net contribution if it is integrated within symmetric boundaries. The calculated magnetic flux is $\Phi \approx 3.16 \times 10^{-8}Vs$, it varies less than 2% over the current period. This value is in good agreement with the flux $\Phi_{theory} = 3.18 \times 10^{-8}Vs$ from a homogeneous flux density $B = 10mT$ multiplied by the image area ($2551.4\mu m \times 1247.0\mu m$). This is another indication for the magneto-optical imaging technique being quantitatively correct.

Because of the nonlinear calibration function, the error in the magnetic field is not straightforward to estimate: based on the results from the frequency dependent measurements (see insets of Fig. 26), one can assume an error in intensity of about ± 0.45 (on a scale of $0 \dots 255$) for the lowest intensity values and of about ± 6.5 for the values at the peaks. After calibration this gives an asymmetric error in the B-field at low intensities

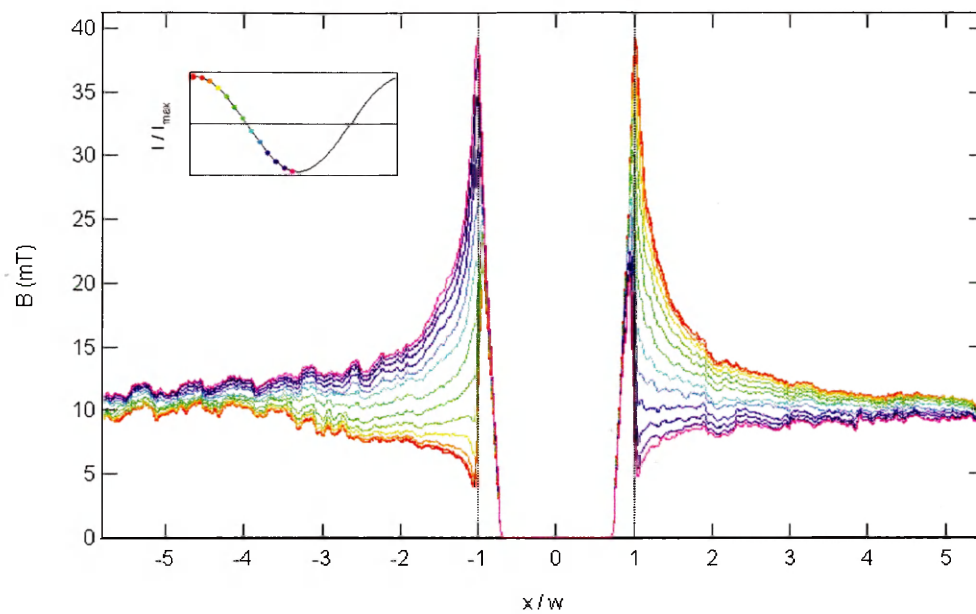


Figure 35: B-field profiles for the first half of the current period.

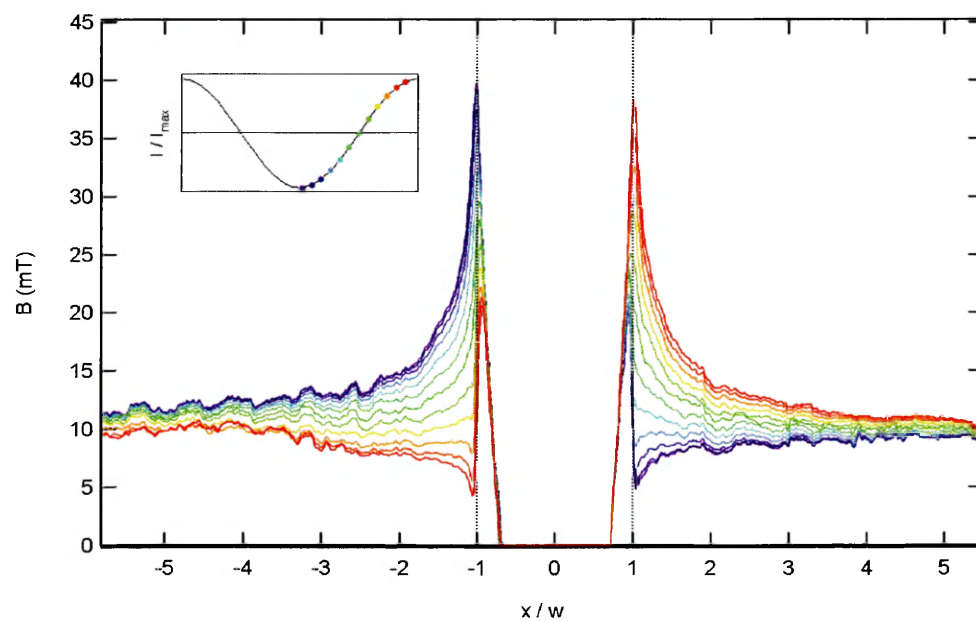


Figure 36: B-field profiles for the second half of the current period.

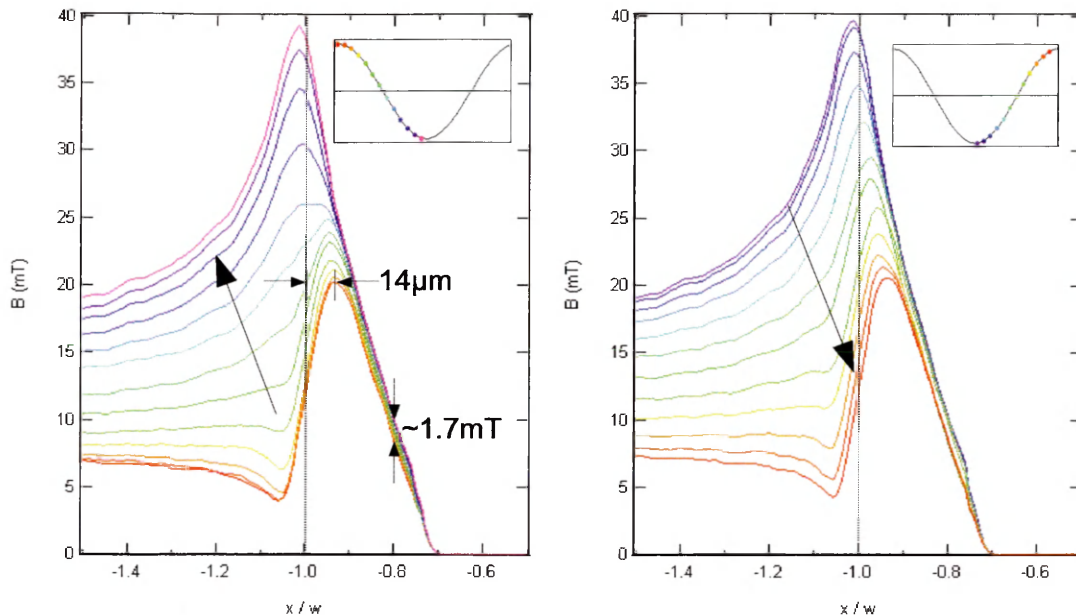


Figure 37: B-field profiles with focus on one sample edge for both half cycles.

$\Delta B_{low,+} = 1.2mT$ and $\Delta B_{low,-} = 2.4mT$. For the peak intensity the error is approximately symmetric with $\Delta B_{peak} \approx 2.3mT$. The average error in the magnetic field is then estimated with $\Delta B \approx \pm 2.0mT$.

Current Density — The current distribution in the sample is calculated from the B-field profiles by inverting the Biot-Savart law. The inversion procedure is described in the appendix B, it yields the current density in a thin film integrated over the film thickness d in units A/m . In the inversion a distance between the sample and the indicator of $h = 0.01w = 2.35\mu m$ has been assumed, which is justified during the following comparison with the model.

The resulting phase dependent current density profiles are shown in Figs. 38 and 39. The current density has the structure of a shielding current as predicted by the critical state model, to which a time dependent transport current is added. The distribution of the transport current is not homogeneous, as shown by the different spread of the profiles between maximum and minimum transport current at different positions on the sample. The current density that appears to be non zero outside the sample is an artifact that can

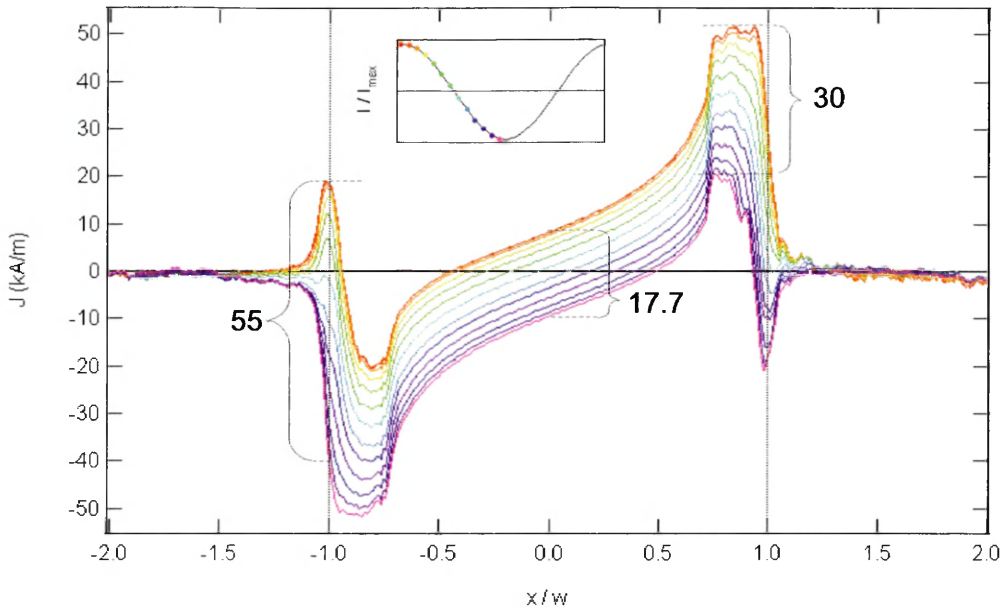


Figure 38: Current density profiles for the first half of the current phase.

be attributed to the smoothing effect of the distance h between sample and indicator.

The current density profiles in Figs. 38 and 39 are integrated in the range $-1 \leq x/w \leq +1$, in order to obtain the time dependent transport current through the sample. The integrated current is shown in Fig. 40 together with the expected sine current with amplitude $8.54A$.

The current obtained by integration of the MOI profiles appears to have an amplitude that is significantly lower than what is expected from the applied current. It can be fit with a sine wave with amplitude $I_{max} = 5.92A$ and a y-axis offset $I_0 = -0.38A$, which is a reduction in AC current of about 30%. It is not entirely clear what the origin of this discrepancy is. An obvious explanation would be, that part of the transport current has bypassed the sample over a shortcut through the cryostat. However, all current carrying wires were electrically isolated, and the sample itself is superconducting so that a normal conducting shortcut parallel to the sample would not divert much current from it.

Another reason for the reduced transport current can be an underestimation of the distance h between the indicator and the sample in the inversion. A larger distance would

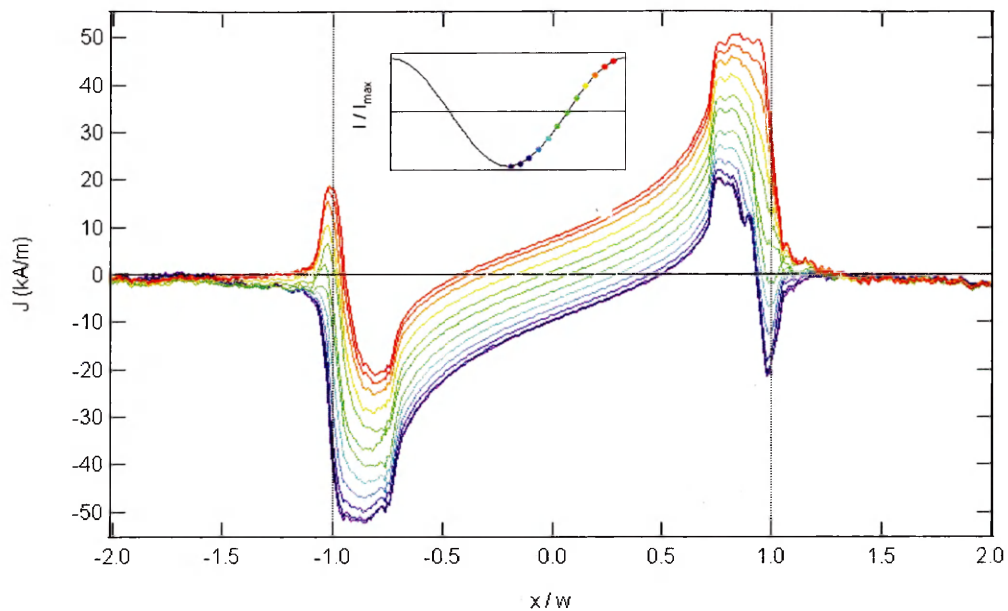


Figure 39: Current density profiles for the second half of the current phase.

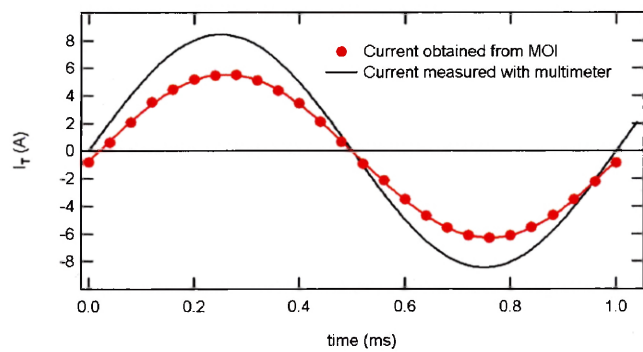


Figure 40: AC current through the sample. Black: applied current in the experiment, with an amplitude of 8.54A. Red: current obtained by integration of MOI current density profiles, with an amplitude of 5.92A.

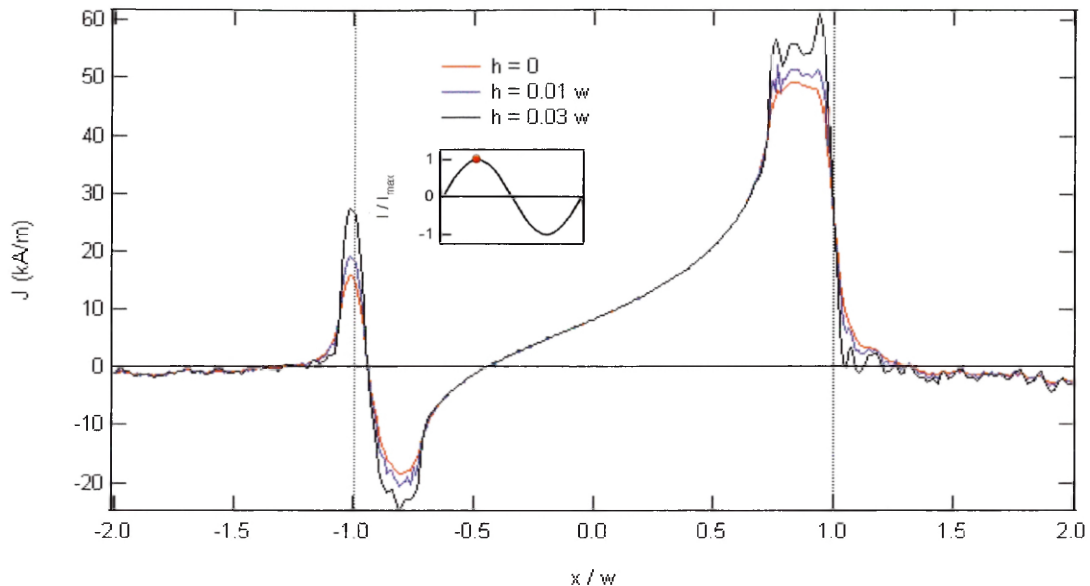


Figure 41: Current density profile calculated assuming different values for the distance between h sample and indicator. $h = 0.01w \approx 0.35\mu m$.

lead to higher current density values, since the current needed to create a certain observed magnetic field in the indicator is higher when the indicator is farther away from the sample. The increase in the current density if a higher value of h is used in the inversion is shown in Fig. 41. However, the increase in current density with h is only small for reasonable $h < 20\mu m$ and this can not completely account for the current discrepancy. The value $h = 0.01$ used in the inversion above is determined in the following modeling section. The question of the reduced transport current remains open.

Modeling — The predictions of the model described in Sec. 2.3 are compared to the experimental results by fitting the theoretical magnetic flux distribution to the measured ones obtained at five different phase points. The parameters entering the model are the transport current I_T , the critical current density J_c in the form of the characteristic field for thin film geometry $B_f = d\mu_0 J_c / \pi$, the applied field B_a as well as the sample-indicator-distance h . The fitted and the experimental magnetic profiles at the five selected phase points as well as the corresponding current density profiles are shown in Figs. 42 to 53.

From the fits at all phase points a characteristic field $B_f = 12mT$ is found. Assuming a sample thickness of $d = 300 \pm 50nm$ this gives a critical current density $J_c = (10.0 \pm 1.7) \times 10^{10}A/m^2$. The parameter h has the effect of smoothing out the singularities in the B-field distribution at the sample edges, it is determined so that the smoothed peaks in the theoretical curves fit the experimental peaks best. From the fits, a distance $h = 0.01w = 2.35\mu m$ is obtained.

In Figs. 42 and 43 the experimental field profiles at the maximum and the minimum phase of the transport current are shown, together with theoretical curves obtained using the applied current $I_T = \pm 8.54A$. In Figs. 46 and 48 the same curves are shown using the transport current $I_T = \pm 5.92A$ obtained by integrating the MOI current density profiles at the respective phase points (plotted in Fig. 40). Comparing Figs. 42 and 46 and Figs. 43 and 48 one finds that the overlap of the model curves with the experimental ones is significantly better if the MOI integrated current at those phase points is used. In Figs. 42 and 43 the field due to the transport current is overestimated, especially outside the sample and in the lower peak at both phase points. This indicates, that the current obtained from the MOI current density profiles is the true transport current through the sample, and that there has been a shortcut that diverted some current from the sample.

In the following the flux density profiles calculated from the model assuming the MOI integrated current are compared to the experimental curves, as shown in Figs. 46 to 48. Generally it is found that the model explains the data reasonably well. In detail one finds that

- the B-field outside of the sample at $|x|/w \geq 1.4$ is described very well by the model at all phase points.
- the flux penetration front at $x \approx 0.73w$ is reproduced well.
- the height of the lower one of the two major peaks near the sample edges is reproduced well at most phase points. The higher peaks seem to be overestimated in the model.

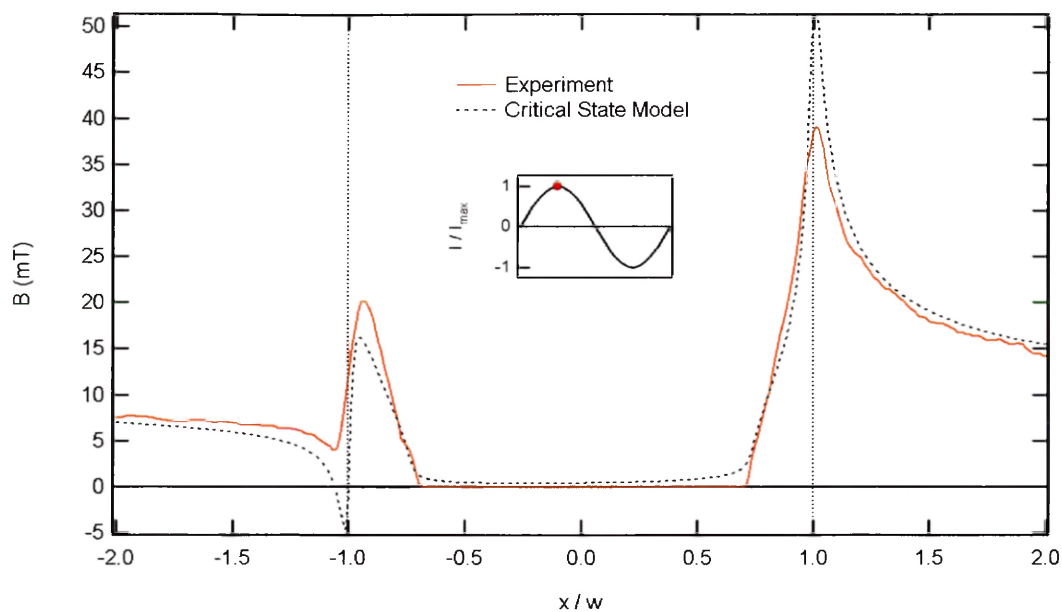


Figure 42: Experimental and theoretical flux density profile at maximum transport current. The theoretical curve is calculated assuming a current $I_T = 8.54A$.

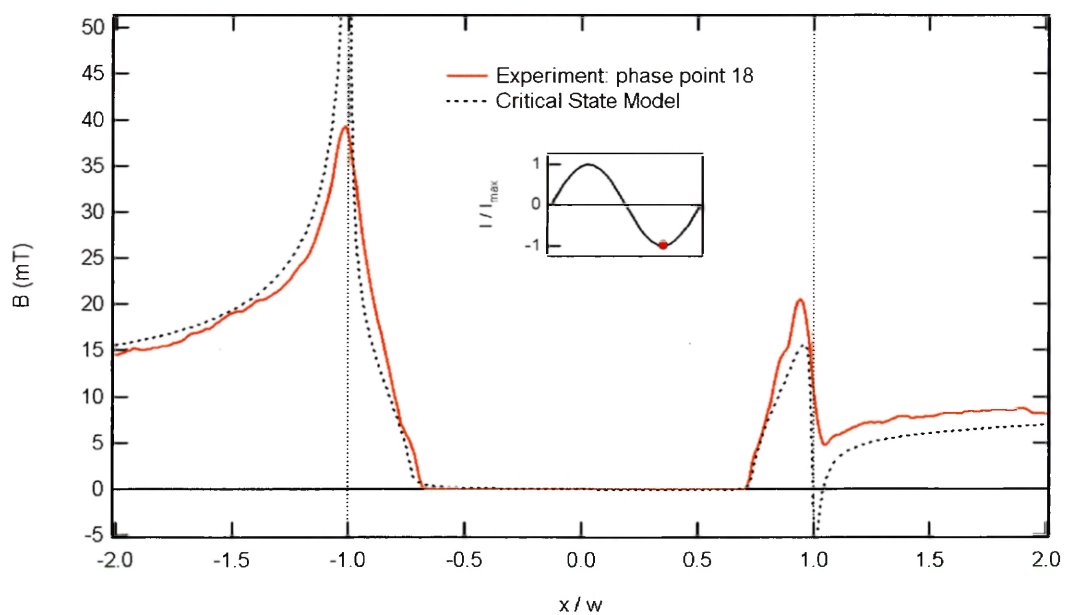


Figure 43: Experimental and theoretical flux density profile at minimum transport current. The theoretical curve is calculated assuming a current $I_T = -8.54A$.

- the lower peaks are shifted inside the sample by about $0.05w$.
- the experimental flux density in a region of about $0.2w$ from the sample edge is higher than predicted by the model. The maximum difference between model and experiment in this region is about $5.5mT$.

The observed shift of the peaks and the increased flux density in the sample show, that the flux that is penetrating the sample is higher than predicted by the model. This increased flux penetration could be explained with thermally activated flux creep into the sample, which is not included in the model. Flux creep has not been observed to cause a frequency dependent effect (see previous section 4). If it causes a higher flux penetration into the sample as proposed here, this means that flux creeps very quickly and the timescale for the additional flux to enter the sample is much shorter than the AC current frequency.

Comparing the theoretical and the experimental current density profiles in Figs. 49 to 53 one finds that

- there is good overall agreement between model and experimental curves in the field free region in the sample center at all phase points.
- at all phase points the smaller one of the two major peaks shows the rounded shape that is also predicted by the model.
- the peaks in the experimental current density profile at zero phase point (see Fig. 49) are narrower and higher by about 20% ($6kA/m$) than predicted. Also the smaller ones of the two peaks at other phase points are larger than the theoretical prediction by about this amount. This can be due to the observed increase in the amount of magnetic flux inside the sample, which increases the shielding current density at the peaks.
- the higher peaks do not show a pronounced trace of the singularity in the theoretical current density. This can be explained with the distance between sample and

indicator, which rounds the high and thin peaks in the current density at the sample edges.

In general it is found that the model predicts the results well. The basic assumption of the model is, that the transport current distributes in such a way, that the self field inside the sample is zero. Because the self field is zero, the shielding current distribution that results from an external magnetic field is not influenced by the transport current, and the total current density distribution is simply the addition of the transport current and the shielding current. The magnetic field profiles that result from current distributions based on this simple assumption are in good agreement with our measurements.

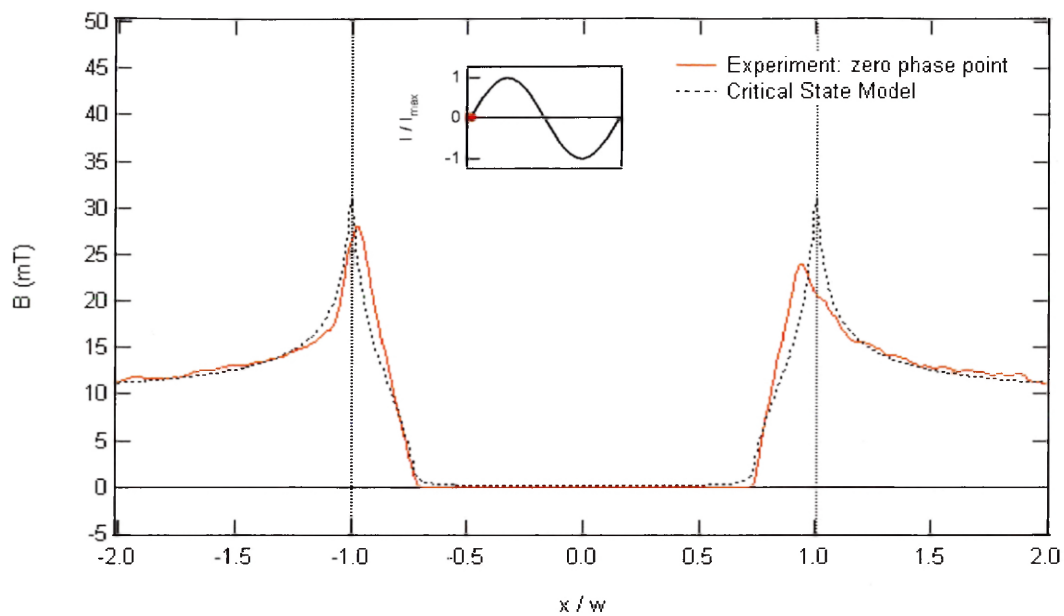


Figure 44: Experimental and theoretical flux density profile at zero transport current.

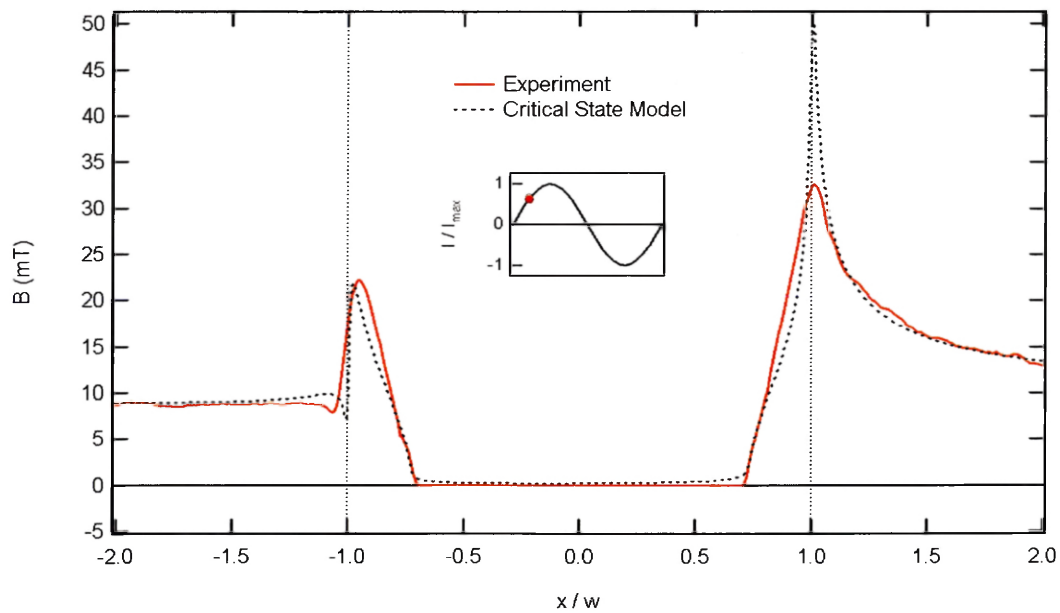


Figure 45: Experimental and theoretical flux density profile at intermediate transport current.

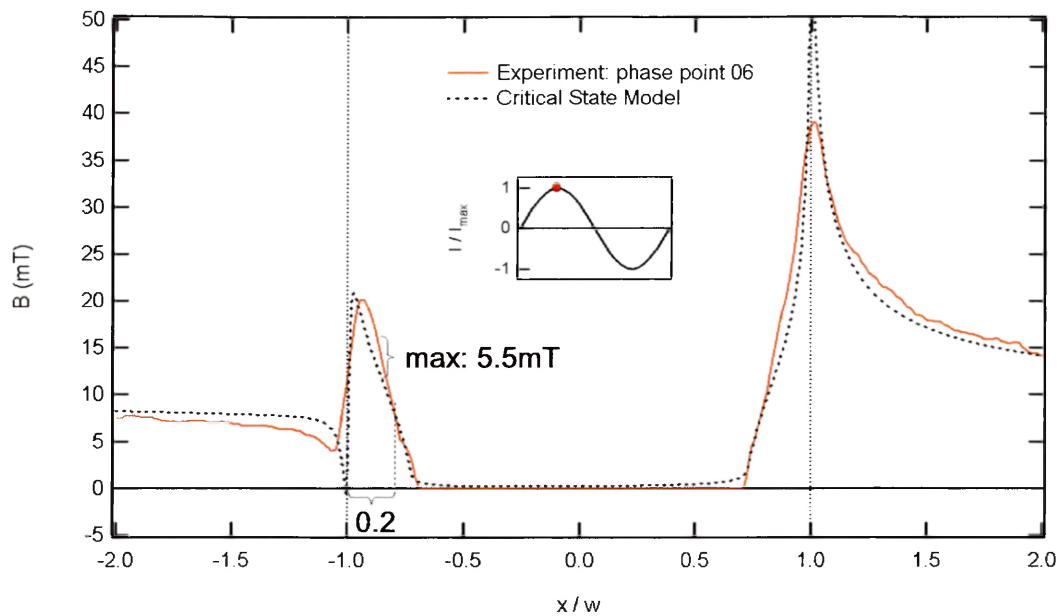


Figure 46: Experimental and theoretical flux density profile at maximum transport current. The range where the experiment shows a higher flux penetration than predicted by the model is marked, as well as the maximum difference in this region between the experimental and the theoretical flux density.

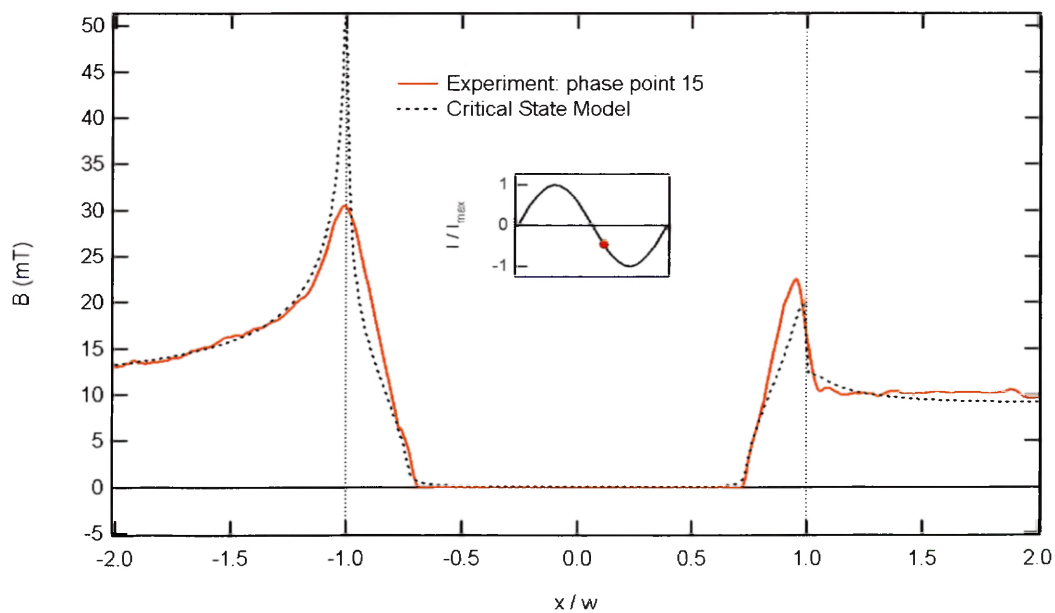


Figure 47: Experimental and theoretical flux density profile at negative intermediate transport current.

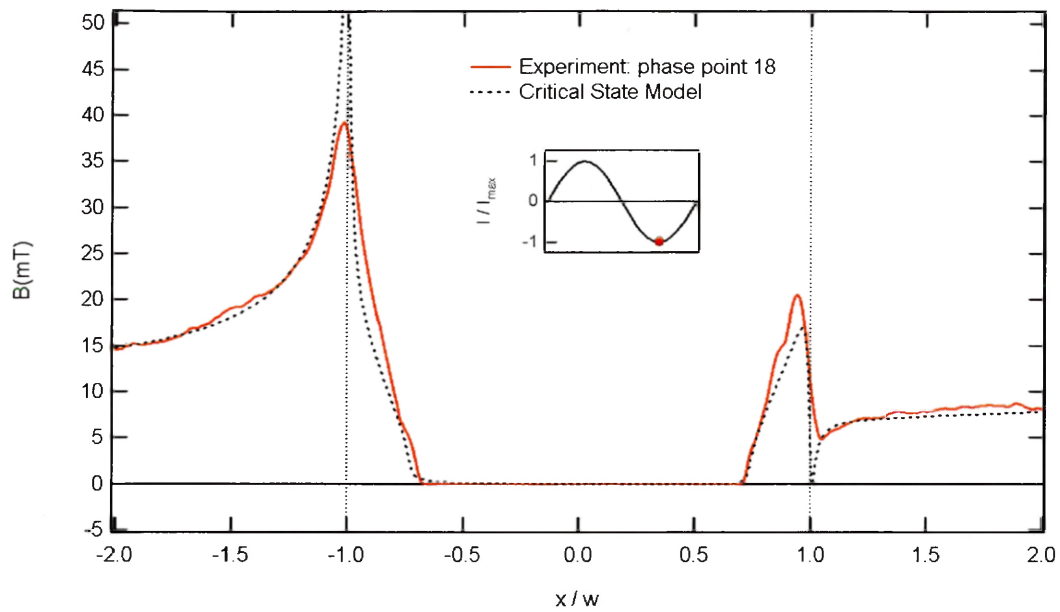


Figure 48: Experimental and theoretical flux density profile at minimum transport current.

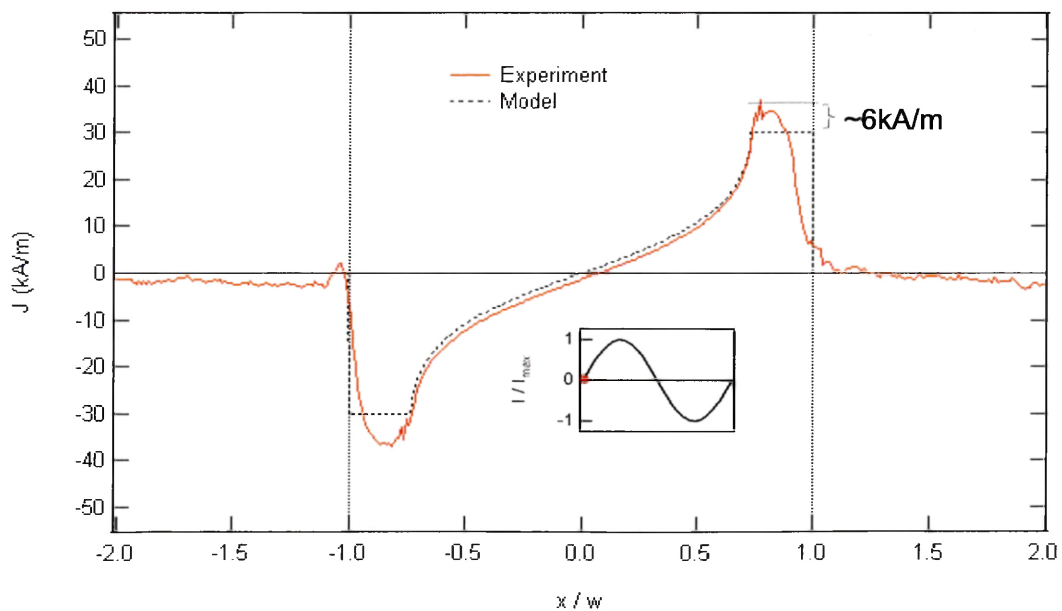


Figure 49: Experimental and theoretical current density profile at zero transport current.

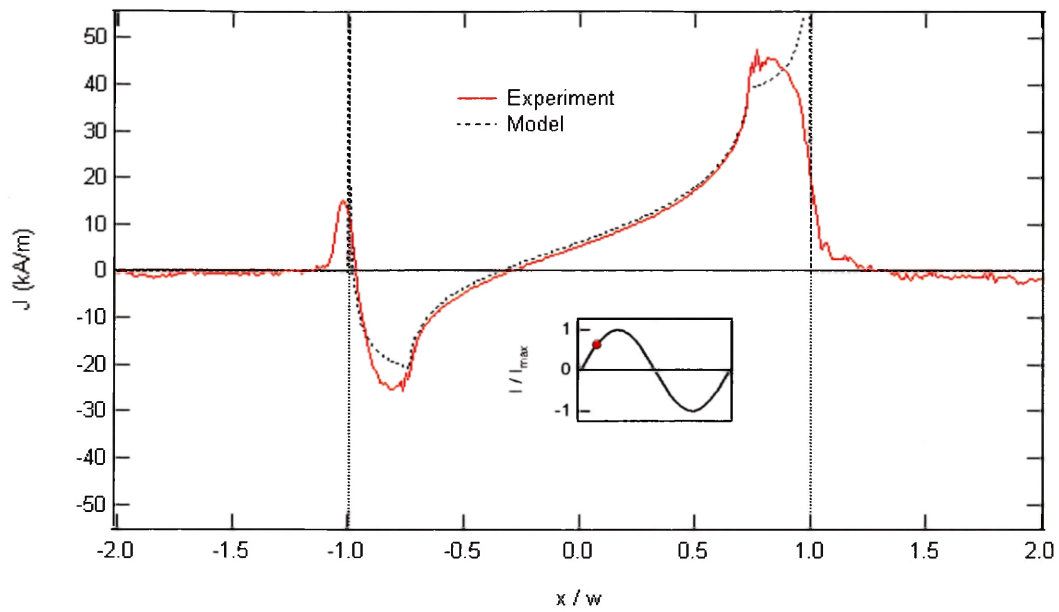


Figure 50: Experimental and theoretical current density profile at intermediate transport current.

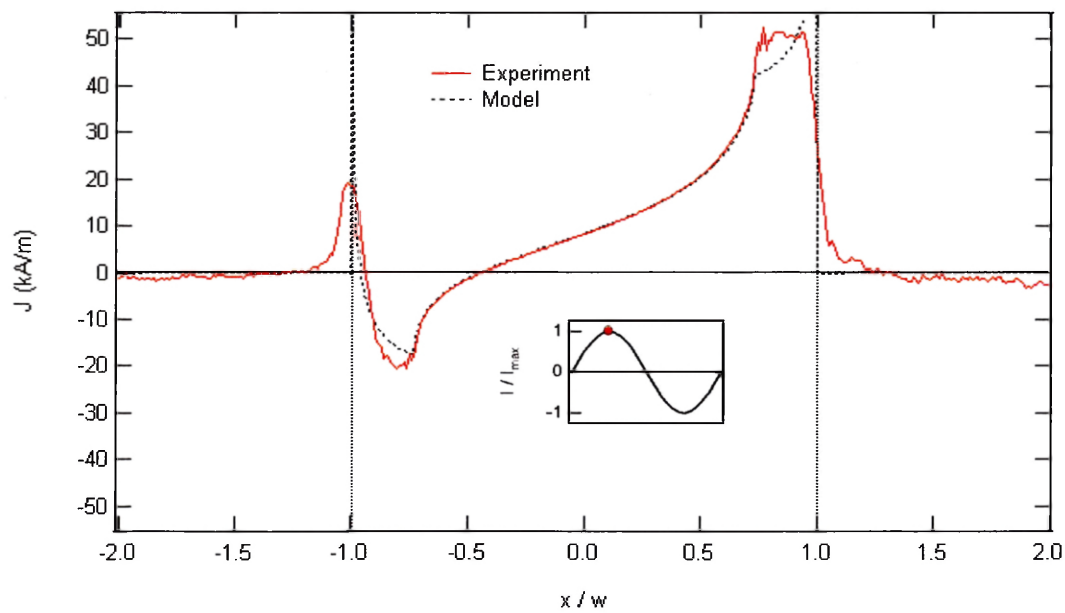


Figure 51: Experimental and theoretical current density profile at maximum transport current.

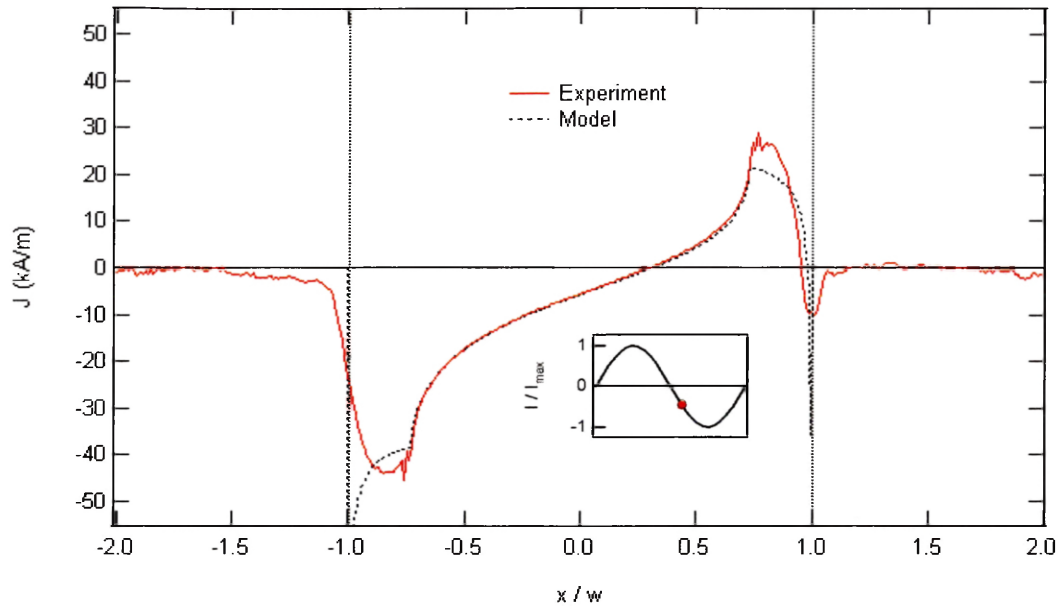


Figure 52: Experimental and theoretical current density profile at negative intermediate transport current.

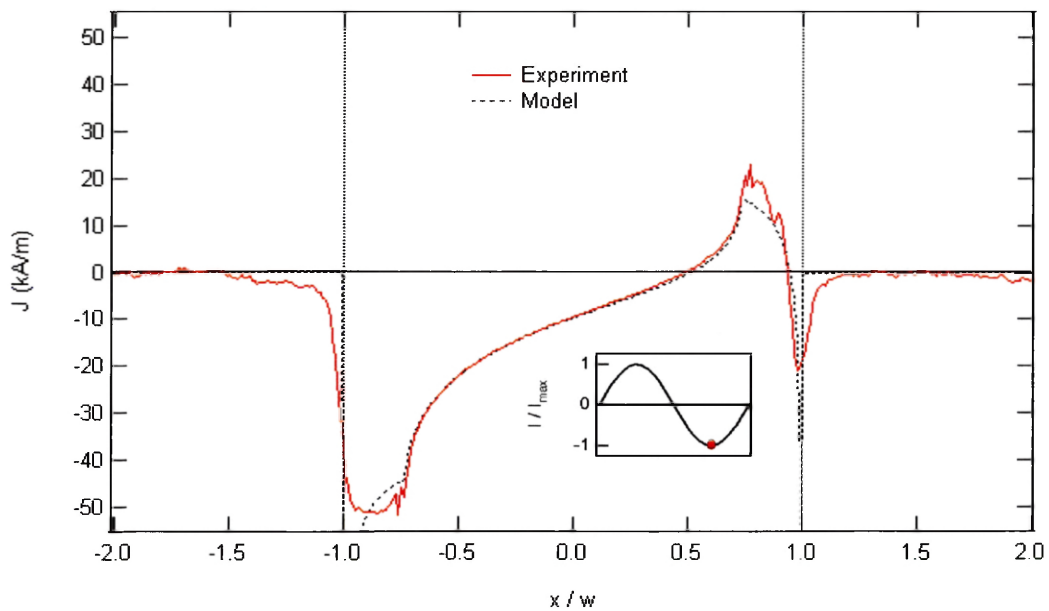


Figure 53: Experimental and theoretical flux density profile at minimum transport current.

6 Conclusions

The spatial magnetic field distribution in a YBCO thin film in the high frequency AC current regime has been studied with time-resolved quantitative magneto-optical imaging at $T \approx 24K$.

It has been found that in the frequency range $100Hz \dots 1000Hz$ the magnetic field distribution shows no appreciable dependence on the frequency of the applied current.

A study of the magnetic flux and the current distribution as a function of the phase of the applied current has been done. It shows that flux jumps do not occur at any point of the phase. The time dependent magnetic field distribution in the sample can be described by a model which assumes, that the self-field of the transport current inside the sample is zero, and that the total current distribution can be described as the sum of a shielding current and the transport current distribution.

The observed differences between the model and the results can be attributed to thermally activated flux creep into the sample.

Appendix A — Synchronization

Figures 54 and 55 show the schematics of the two synchronization stages.

Both delay stages use 15-turn potentiometers with a resistance $0\Omega \leq R \leq 100k\Omega$. In the first stage 12 different capacitances C with $50nF \leq C \leq 1\mu F$ can be selected corresponding to 12 delay ranges $\Delta\phi_{max}$ between $1.1ms$ and $110ms$. This variety of capacitances ensures that for frequencies in the range $20Hz \leq f \leq 1000Hz$ a maximum time delay approximately equals the AC current period is always available, which allows fine control of the delay over the whole period using the full range of the potentiometer. The second delay stage features only two capacitances because this delay does not have to be as finely tunable as the first one, since it is just added the first one as a constant.

The circuit is powered by a $\pm 12V$ DC voltage, which is stabilized against voltage peaks originating from within the circuit, as shown in Fig. 56.

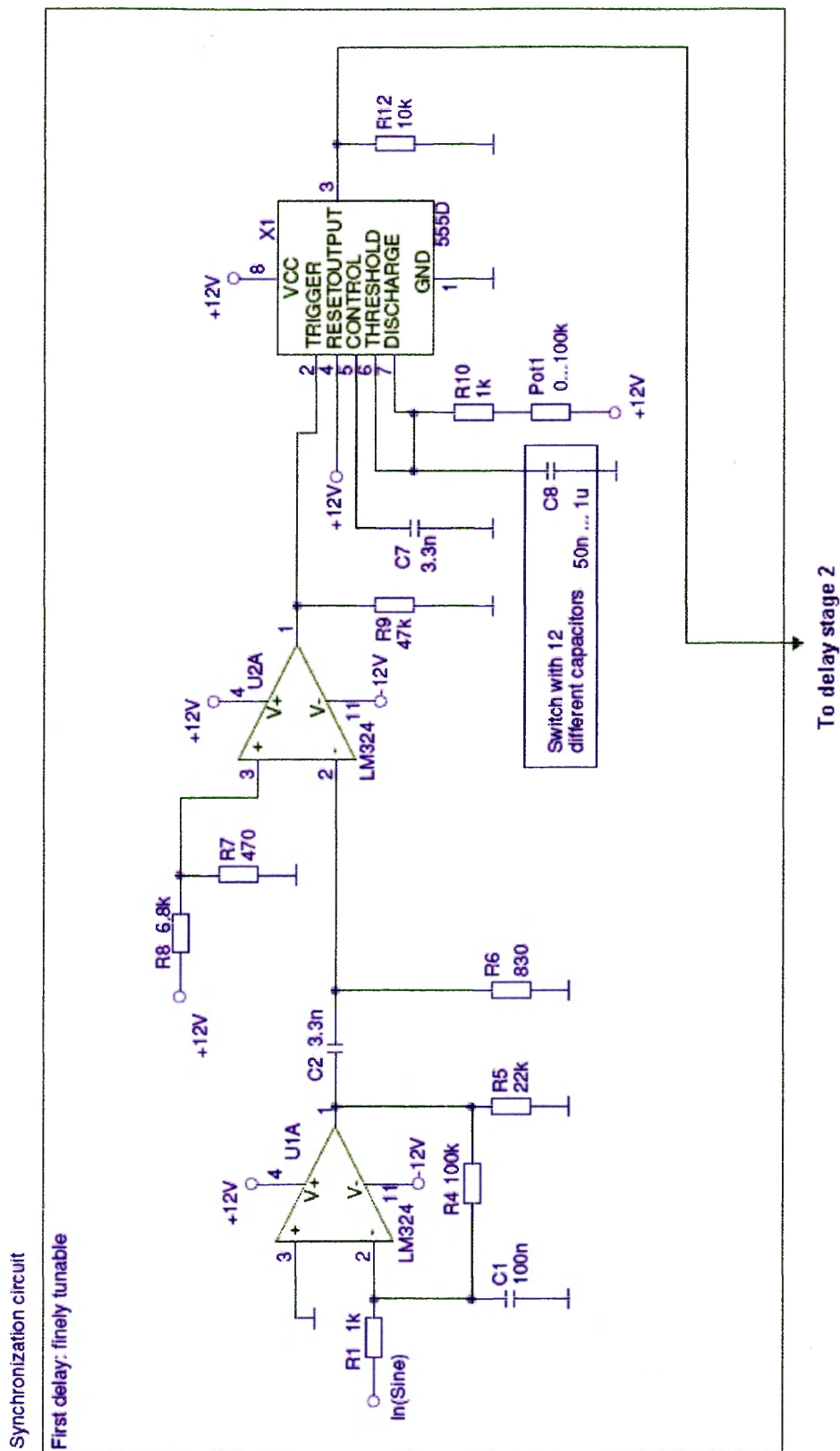


Figure 54: Schematic of the first delay stage

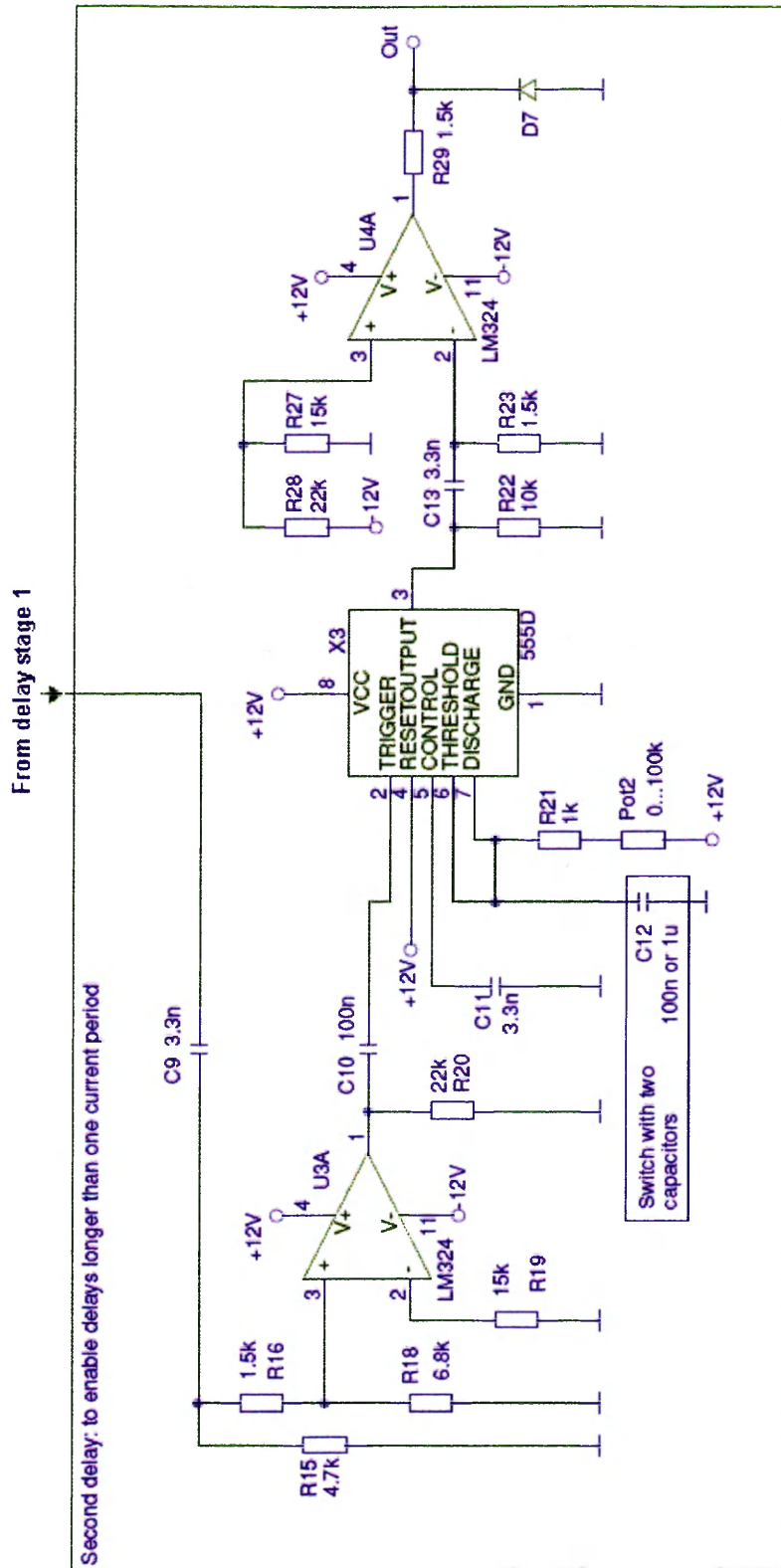


Figure 55: Schematic of the second delay stage

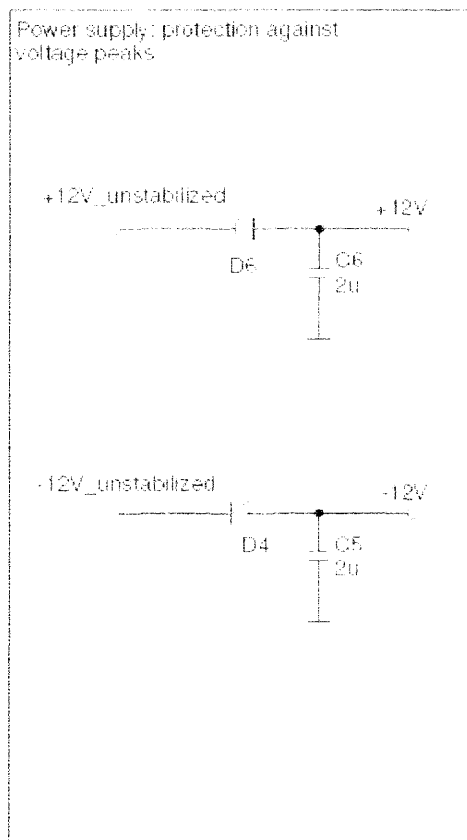


Figure 56: Schematic of the stabilization of the power supply for the synchronization

Appendix B — Inversion

This section describes the method used to obtain the current density profile in a thin film sample, by measuring the magnetic field distribution at a distance h above the film. Let a one-dimensional current density $j_y(x)$ flow along the y direction in the x-y-plane. The perpendicular magnetic field $B_z(x, h)$ created by this current at a distance h above the x-y-plane is given by the Biot-Savart-law

$$B_z(x, h) = \frac{\mu_0}{2\pi} \int_{-\infty}^{\infty} \frac{j_y(x')(x - x')}{(x - x')^2 + h^2} dx'. \quad (28)$$

Discretizing the integral on a grid of N points x_n , corresponding to the number of pixels in a profile, gives

$$B_z(x_m, h) = \frac{\mu_0}{2\pi} \sum_{n=0}^N \frac{j_y(x_n)(x_m - x_n)}{(x_m - x_n)^2 + h^2} \Delta x \quad (29)$$

where Δx is the distance corresponding to the width of one pixel. The integral kernel, which consists solely of geometric terms, is a square matrix of size $N \times N$

$$(M)_{m,n} = \frac{x_m - x_n}{(x_m - x_n)^2 + h^2} \Delta x. \quad (30)$$

The discretized Biot-Savart law can then be written as a matrix equation, where the discrete line profiles of the magnetic field and current density are vectors of dimension N

$$\mathbf{B}_z = \frac{\mu_0}{2\pi} \mathbf{M} \cdot \mathbf{j}_y. \quad (31)$$

If two slightly different discretization grids for the current and the B-field are used, such that $x_m \neq x_n$ for all n, m , the diagonal elements of \mathbf{M} are non-zero and the matrix can be inverted. One then gets the discretized one-dimensional current distribution in a thin film, that creates a given magnetic field profile at a distance h above the film

$$\mathbf{j}_y = \frac{2\pi}{\mu_0} \mathbf{M}^{-1} \cdot \mathbf{B}_z. \quad (32)$$

The larger the distance h between the indicator and the sample is, the more the magnetic field distribution in the indicator plane is smoothed. On the other hand, small noise in a measured B-field profile becomes greatly amplified during the inversion to a current distribution, if h is large. The threshold in h below which one obtains reasonable current density profiles without too much noise is about $h \leq \Delta x \approx 2.5\mu m$.

References

- [1] M.W. Rupich et. al. YBCO coated conductors by an MOD/RABiTS/spl trade/process. *IEEE Transactions on Applied Superconductivity*, 13:2458, 2003.
- [2] P. N. Barnes, M. D. Sumption, and G. L. Rhoads. Review of high power density superconducting generators: Present state and prospects for incorporating YBCO windings. *Cryogenics*, 45:670, 2005.
- [3] P.N. Barnes, G.L. Rhoads, J.C. Tolliver, M.D. Sumption, and K.W. Schmaeman. Compact, lightweight, superconducting power generators. *IEEE Transactions on Magnetics*, 41:268–273, 2005.
- [4] Ch. Jooss, J. Albrecht, H. Kuhn, S. Leonhardt, and H. Kronmüller. Magneto-optical studies of current distributions in high-Tc superconductors. *Rep. Prog. Phys.*, 65:651–788, 2002.
- [5] T. H. Johansen, M. Baziljevich, H. Bratsberg, Y. Galperin, P. E. Lindelof, Y. Shen, and P. Vase. Direct observation of the current distribution in thin superconducting strips using magneto-optic imaging. *Phys. Rev. B*, 54:16264, 1996.
- [6] M. E. Gaevski, A. V. Bobyl, D. V. Shantsev, Y. M. Galperin, T. H. Johansen, M. Baziljevich, H. Bratsberg, and S. F. Karmanenko. Magneto-optical study of magnetix-flux penetration into a current-carrying high-temperature-superconductor strip. *Phys. Rev. B*, 59:9655–9663, 1999.
- [7] C. P. Bean. Magnetization of hard superconductors. *Phys. Rev. Lett.*, 8:250, 1962.
- [8] E. Zeldov, J. R. Clem, M. McElfresh, and M. Darwin. Magnetization and transport currents in thin superconducting films. *Phys. Rev. B*, 49, 1994.
- [9] E. H. Brandt and M. Indenbom. Type II superconductor strip with current in a perpendicular magnetic field. *Phys. Rev. B*, 48, 1993.

- [10] I. A. Rudnev, D. V. Shantsev, T. H. Johansen, and A. E. Pirmenko. Avalanche-driven fractal flux distributions in NbN superconducting films. *Appl. Phys. Lett.*, 87:042502, 2005.
- [11] A. Lucarelli, G. Lüpke, G. A. Levin, and P. N. Barnes. Time-resolved magneto-optical imaging of YBCO thin films in high-frequency AC current regime. *Supercond. Sci. Technol.*, 19:667670, 2006.
- [12] R. Liang, P. Dosanjh, D. A. Bonn, W. N. Hardy, and A. J. Berlinsky. Lower critical fields in an ellipsoid-shaped YBaCuO single crystal. *Phys. Rev. B*, 50:4212–4215, 1994.
- [13] W. Buckel and R. Kleiner. *Superconductivity - Fundamentals and Applications*. Wiley - VCH, 2004.
- [14] K. Fossheim and A. Sudbo. *Superconductivity - Physics and Applications*. John Wiley and Sons, 2004.
- [15] Rafael B. Dinner, M. R. Beasley, and Kathryn A. Moler. Cryogenic scanning Hall-probe microscope with centimeter scan range and submicron resolution. *Rev. Sci. Instrum.*, 76:103702, 2005.
- [16] Y. Abulafia, Y. Wolfus, M. McElfresh, A. Shaulov, Y. Yeshurunc, Y. Paltiel, H. Shtrikman, and E. Zeldov. Hall-array gradiometer for measurement of the magnetic induction vector in superconductors. *J. Appl. Phys*, 85:5471, 1999.

Vita

Alexander Frey has been born in Kuenzelsau, Germany on February 16, 1982. He graduated from Ganerben Gymnasium (highschool) in Kuenzelsau in 2001. He received his B.Sc. at Wuerzburg University, Germany in 2004 in physics. He pursued graduate studies in physics at Wuerzburg University until July 2005.

In August 2005, the author entered the College of William and Mary as a graduate research assistant in the Department of Applied Science. Alexander Frey defended his M.Sc. thesis in July of 2006.